# PPARγ mediated enhanced lipid biogenesis fuels *Mycobacterium tuberculosis* growth in hepatocytes.

**Binayak Sarkar[1], Jyotsna Singh[1], Mohit Yadav[1], Priya Sharma[2], Raman Deep Sharma[2], Shweta Singh[3], Aakash Chandramouli[4], Ashwani Kumar[3], Siddhesh S. Kamat[4], Devram S. Ghorpade[1], Debasisa Mohanty[1], Dhiraj Kumar[2], Rajesh S. Gokhale[1,4, #].**

**1** Immunometabolism laboratory, National Institute of Immunology, New Delhi, India, **2** Cellular Immunology Group, International Centre for Genetic Engineering and Biotechnology, New Delhi, India **3** CSIR-Institute of Microbial Technology, Chandigarh, India, **4** Indian Institute of Science Education and Research, Pune, Maharashtra, India.

**#** Current address: Indian Institute of Science Education and Research, Pune, Maharashtra, India.

**Keywords:** Liver, Mtb, hepatocytes, PPARγ, anti-TB drugs, lipid droplets.

**Corresponding author:** Rajesh S. Gokhale (rsg@nii.ac.in)

**Abstract**

*Mycobacterium tuberculosis* (Mtb) infection of the lungs, besides producing prolonged cough with mucus, also causes progressive fatigue and cachexia with debilitating loss of muscle mass. While anti-tuberculosis (TB) drug therapy is directed towards eliminating bacilli, the treatment regimen ignores the systemic pathogenic derailments that probably dictate TB-associated mortality and morbidity. Presently, it is not understood whether the spread of infection to other metabolic organs brings about these impairments. Here, we show that Mtb, during the chronic phase utilizes hepatocytes as a replicative niche and shields itself against the common anti-TB drugs by inducing drug-metabolizing enzymes. Mtb creates a replication-conducive milieu of lipid droplets in hepatocytes by upregulating transcription factor PPARγ. In the classical murine-TB aerosol infection model, hepatocyte infection can be consistently observed post-week 4 along with enhanced expression of PPARγ and drug-metabolizing enzymes. Histopathological analysis and fluorescence in situ hybridization with Mtb-specific primers of human autopsy liver specimens, indeed show the presence of Mtb in hepatocytes along with granuloma-like structures. Hepatotropism of Mtb during the chronic infectious cycle results in immuno-metabolic dysregulation that could magnify local and systemic pathogenicity, altering clinical presentations.

.

## Introduction

*Mycobacterium tuberculosis* (Mtb), the causative agent of human tuberculosis, remains the leading infectious killer globally with an estimated death of 1.3 million in 2022[1]. Despite progressive work on designing new anti-TB therapeutics and implementing vaccination programs in TB-endemic countries, it has a high global case fatality rate and a poor treatment success rate, along with a rising number of drug-resistant infections[2, 3]. Emerging paradigms strongly suggest that chronic infectious diseases cannot be tackled as one-dimensional problems that can be solved by the elimination of pathogens alone. A holistic understanding of how the host systems respond to the infection, vaccination, and treatment is key to TB management programs[4]. Recent widespread and severe physiological derangements associated with COVID-19 patients, even after the elimination of the virus, have brought back the focus on identifying novel strategies that are inclusive of modulating the host immune-metabolic axis[5, 6].

The clinical symptoms of pulmonary TB encompass localized manifestations like prolonged cough with mucus, pleuritic chest pain, hemoptysis, lung damage etc. Besides, systemic outcomes like cachexia, progressive fatigue, oxidative stress, altered microbiota, glucose intolerance, etc. result in organ-wide disruptions[7, 8]. Pulmonary TB patients often suffer from progressive and debilitating loss of muscle mass and function with severe weight loss, this TB-associated cachexia cannot be reversed by conventional nutritional support[9, 10]. Besides, numerous epidemiological studies indicate that hyperglycemia may occur during active tuberculosis, which can compromise insulin resistance and glucose tolerance, although the mechanisms are unclear[7, 11, 12]. Both the localized and systemic pathophysiology of TB infection indicates an alteration in the

host immuno-metabolic axis. It is somewhat bewildering that engagement of liver during Mtb infection cycle is not considered, despite its central role in balancing immune and metabolic functions of the body[13]. The crosstalk between the liver and lung has been largely overlooked in tuberculosis (TB), even though acute phase proteins (APPs) are used as predictive biomarkers in pulmonary tuberculosis[14]. A robust hepatic acute phase response in mice, mediated by key hepatocyte transcription factors, STAT3 and NF-κB/RelA, has been to trigger pulmonary host defenses for survival during pneumonia and sepsis[15]. In TB, the active phase of the disease is associated with heightened expression of interferon-inducible genes that modulate flux in the lipid metabolic pathway[16, 17].

The liver is involved in a wide variety of functions – synthesis, secretion, degradation, and regulation[18, 19]. De-novo lipogenesis, secretion of acute phase proteins, hepatokine production, etc. are all directly or indirectly controlled by the hepatocytes, thereby communicating with almost all the organs of the body[20]. To avert organ damage, the liver maintains tolerogenic properties rendering it an attractive target for various pathogenic microorganisms. *Plasmodium*. spp, the causative agent of malaria uses hepatocytes to replicate robustly before infecting the erythrocytes[21, 22]. Besides, various viruses like Hepatitis B, C, and E infect the hepatocytes and establish a chronic state of infection[23, 24]. Furthermore, most studies regarding TB drug resistance have focused primarily on the Mtb factors, but the role of the host organs in drug tolerance and resistance is underappreciated[25].

In this study, we demonstrate the active involvement of the liver in a murine aerosol TB infection model during the chronic phase and establish hepatocytes as a new replicative

niche for Mtb. Using a variety of *in vivo*, *ex vivo*, and *in vitro* techniques we show how Mtb perturbs biological functions within hepatocytes remodeling intracellular growth, localization, and drug sensitivity. Cellular and mass spectrometric studies demonstrate Mtb infection-mediated enhanced fatty acid biogenesis and TAG biosynthesis in the hepatocytes regulated by PPARγ. We propose that infection of hepatocytes by Mtb during the chronic phase can contribute to significant changes in disease progression, TB treatment, and development of infection-induced metabolic diseases.

## Results

### Human pulmonary tuberculosis patients harbor Mtb in the liver.

Mtb infects lungs, and other organs like lymph nodes, pleura, bone, meninges, etc. There are also few case reports of hepatic TB, without providing much pathophysiological consequences[26, 27]. To gain further insights into the involvement of the liver in Mtb infections, we acquired human autopsied liver samples from the Postgraduate Institute of Medical Education and Research (PGIMER), Chandigarh, India. These samples were then analyzed for the presence of Mtb bacilli and histological features of TB. Hematoxylin and eosin (H and E) staining showed the presence of distinct immune cell infiltration and granuloma-like structures in the infected samples (Fig 1A and Fig S1C). Hepatic granuloma can occur due to a wide range of etiologies like primary biliary cirrhosis, infectious disease, foreign bodies, neoplasms, drug toxicity, etc.[27]. To validate the presence of Mtb in the liver specimen having characteristic granulomas, Mtb-specific staining of auramine O- rhodamine B and Ziehl-Nielsen (Z-N) acid-fast were conducted (Fig 1B, C). In both cases, there were distinct positive signals for both auramine-

rhodamine and acid-fast staining with recognizable Mtb-like structures in the acid-fast sections. We further corroborated our findings by performing fluorescence in-situ hybridization (FISH) using Mtb-specific 16s rRNA probes, where specific signals were observed (Fig 1D). Similar staining in the uninfected liver section samples did not show any signal. (Fig S1A, B). Multiplex immunostaining with β-actin and Mtb-specific Ag85B shows the presence of Ag85B within the human hepatocytes further confirming the presence of Mtb within hepatocytes (Fig S1D). Moreover, hepatic granulomas in the human samples showed localized clustering of the immune cells (Fig S1D). Our results, through multiple techniques, confirm the infection of Mtb in the liver in human subjects and show localization of Mtb within the hepatocytes.

**Primary mouse hepatocytes and HepG2 provide a replicative niche to Mtb.**

Mtb infection of the hepatocytes in the human autopsy liver specimens prompted us to investigate the aspect of Mtb survival within hepatocytes. We therefore examined several hepatocyte cell lines of mouse and human origin along with murine primary hepatocytes. Initial infection studies of isolated primary hepatocyte cells (PHCs), HepG2, Huh-7, and AML-12 with labelled-*H37Rv* were performed. Multiplicity of infection (MOI) of 10 showed robust infection with minimal cell death. Macrophage cell lines RAW 264.7 and THP-1 were used as positive controls. Even though PHCs, HepG2, Huh-7, and AML-12 are not considered to be classical phagocytic cells, all cells showed an infectivity of more than 60 percent after 24 hours, comparable to the conventional macrophages (Fig 2A, B). Analysis of bacterial load in the PHCs post-infection showed colony forming units (CFU) like RAW 264.7 and THP-1, supporting microscopic observations (Fig 2C). Mtb in macrophages is known to remodel intracellular environment to survive within

phagosomes[28]. We studied Mtb growth kinetics within hepatocytes using GFP-labeled Mtb *H37Rv* in PHCs and HepG2 (Fig 2D and F). Mean fluorescent intensity measurements showed a consistent increase in GFP intensity in both PHCs and HepG2 with increasing time (Fig 2E and G). CFU enumeration also substantiated microscopic observations of steady Mtb replication (Fig 2F, G). Strikingly, PHCs and HepG2 show better growth rate than RAW 264.7 and THP-1 (Fig 2H-K). While bacterial growth in macrophages plateaus after 48 hours post-infection, Mtb continues to grow in hepatocytes Similar trend is observed for the Mtb BCG vaccine strain (Fig S2A, S2B). Our studies thus establish that hepatocytes, besides being robustly infected by Mtb, also provides a favorable replicative niche for Mtb.

**Transcriptomics of infected hepatocytes reveal significant changes in key metabolic pathways.**

To understand Mtb-induced changes in the hepatocytes and the underlying mechanisms of how hepatocytes provide a favorable environment to the pathogen, we performed transcriptomic analysis of the infected and sorted HepG2 cells at 0 hours (5 hours post incubation) and 48 hours post-infection. Sorting prior to RNA isolation specifically enriches the infected cellular population thus eliminating cellular RNA from uninfected cells (Fig 3A and B). Unsupervised clustering segregated the data into 4 distinct groups on the PC1 with a variance of 27 percent, showing good concordance within the replicates. The close spatial clustering for the two 0-hour time points corresponding to uninfected and infected is indicative of relatively less transcriptomic changes. On the other hand, the spatial segregation of the 48 hours datasets suggests clear differences between the RNA transcripts of uninfected and infected cells. The differentially expressed

genes were calculated using DE seqR with fold change >0.5 and a false discovery rate of <0.2. Gene ontology (GO) enrichment analysis for the differentially regulated pathways at both the early (0 hours) and the late (48 hours) infection time points is shown in (Fig 3D). At 0 hours post-infection, the immediate stress response pathway of the cell, involving ROS generation, intracellular receptor signaling pathways, and response to xenobiotic stresses got activated, while at a late time point, Mtb modulated some of the key immuno-metabolic pathways like macroautophagy, cellular respiration, proteasomal degradation pathway, response to type I interferon, IκB kinase/NF-κB signaling, etc (Fig 3D). Major alterations in the vacuolar and vesicular transport at 48 hours are indicative of the dynamic changes in the phagosome maturation pathway (Fig 3D). Volcano plot analysis showed greater relative changes in the gene expression pattern at 48 hours compared to 0 hours, with many genes like *CXCL10, CXCL11, IDO, CCL5* etc to be greatly upregulated (Fig 3E, 3F). Interestingly, our RNA sequencing data indicated major changes in various facets of lipid metabolic pathways like fatty acid biosynthesis pathway, glycerolipid and glycerophospholipid metabolism, cholesterol biosynthesis pathways etc. Several key genes like *FASN, DGAT1, DGAT2*, *HMGCR*, etc. were upregulated, indicating the possibility of greater synthesis of neutral lipids. Thus, transcriptomic studies shed light on several of the key Mtb-induced changes in the hepatocytes.

**Mtb confines within early phagosome in the hepatocytes.**

To understand the localization of Mtb within hepatocytes, we examined the percentage of colocalization of Mtb-GFP within different sub-cellular compartments. Rab5 and EEA1 were used as early endosomal markers, Rab7 as late endosomal marker, Cathepsin D and LAMP1 as lysosomal markers, lysotracker RED+Cathepsin and lysotracker RED+

LAMP1 served as markers for acidified lysosomes. At 24 hours post-infection, the percent of the bacteria colocalized within the early endosomal markers Rab5 and EEA1 in both PHCs and HepG2 was nearly 60 percent, suggesting that the bacteria restrict to the less acidified compartments. Interestingly, the percentage colocalisation within the late, comparatively more acidic compartments of late endosomes and lysosomes are below 20 percent (Fig 4 A, B and S4A and B). Interestingly, inducing lysosomal acidification by the addition of rapamycin reduces bacterial load in PHCs depicting the presence of a functional phagolysosomal killing machinery operating in hepatocytes (Fig S4C). This data is analogous to the phagosome maturation as observed in conventional macrophages like THP1.Thus, there is a correspondence between the early growth phases of macrophages and hepatocytes, where the bacteria prefer to inhabit within the early-endosomal compartments ensuring their prolonged survival.

**Hepatocytes resident Mtb displays a drug tolerant phenotype.**

The success of Mtb as a pathogen is partially attributed to its ability to survive and adapt to antibiotics[29]. Hepatocytes contain both phase I and phase II drug metabolizing enzymes (DMEs). Further, pharmacological potency of lipophilic drugs is determined by the rate at which these drugs are metabolized to inactive products[30, 31]. Cytochrome P450 monooxygenases (cyp450s) system is the key phase I DMEs and known to interact with rifampicin[32]. We therefore analysed whether Mtb infection influences the cyp genes in hepatocytes. Analysis of the transcriptomics data revealed major changes in several of the key drug modifying enzymes (DMEs) genes (Fig S5B). Of particular interest was *CYP3A4* and *CYP3A43* respectively, both of which metabolize anti-TB drug rifampicin. Quantitative real time PCR of *CYP3A4, CYP3A43* AND *NAT2* genes in infected HepG2

cells showed the genes to be upregulated by almost 4-fold (CYP3A4) and 2-fold (*CYP3A43* and *NAT2)* (Fig S5 C). We therefore argued that hepatocyte resident Mtb may display higher tolerance to rifampicin. Towards this, we treated Mtb infected HepG2 and PHCs with different concentrations of Rifampicin (0.1, 0.5, 5 µg/ml) for 24 hours and CFU enumerated the bacterial after lysis. RAW 264.7 was kept as macrophage control with the similar experimental setup. The percentage of bacteria which survived the drugs was the drug tolerant population. Both HepG2 and PHCs resident Mtb were significantly tolerant to (25-30%) to rifampicin, as compared to the macrophages (Fig 5A and B). Almost 10 percent of the bacterial population in hepatocytes display a tolerogenic phenotype at the highest antibiotic concentration (Fig 5A)

We also examined Mtb susceptibility to isoniazid (INH), which is predominantly metabolized (50–90%) via N-acetylation of its hydrazine functionality by arylamine N-acetyltransferase 2 (*NAT2*)[33]. Interestingly, KEGG analysis of transcriptomic data suggested several genes in this pathway to be upregulated in hepatocytes infected with Mtb (Fig S5B). Experimental studies indeed showed higher tolerance of Mtb to INH in both primary hepatocytes and HepG2 at different concentrations (0.1, 0.5, 5 µg/ml) (Fig 5C). Moreover, transcript levels of some of the key DMEs (were upregulated in the liver of the infected mice, 8 weeks post-infection like *Slco1b2*, *Oct12, Ces1, Ces2, Aadac* (upregulated by almost 2-3-fold) (Fig 5D). Our data show that Mtb-infection of hepatocytes induces DMEs, and this extrinsic activation may result in decreased bioavailability or increased inactivation of anti-TB drugs.

**Increased fatty acid synthesis drives Mtb growth in hepatocytes.**

Mtb survival in foamy macrophages is driven by nutrient acquisition from the lipid droplets[34]. Transcriptomic studies of Mtb infected cells also showed upregulated pathways for lipid metabolism. Examination of Lipid droplets in both PHCs and HepG2 revealed a remarkable increase in the number of lipid droplets at 24 hours post-infection (Fig 6A and B). Time kinetic analysis of BODIPY intensity in the infected HepG2 at different days post-infection indicated a concomitant increase in lipid droplets with the progress of infection (Fig 6C). Most significant difference was noted at 48 hours post-infection (Fig 6C). Lipid droplets are single membrane-bound depots consisting mainly of neutral lipids like diacylglycerols (DAGs), triacylglycerols (TAGs), and cholesterol esters 9 (CEs).

Mass-spectrometric analysis of the infected and uninfected HepG2 cells at 24 hours post-infection, showed an increase in both TAGs and DAGs and CEs with a decrease in the levels of free cholesterols, indicating Mtb-induced changes in the neutral lipid biosynthesis (Fig 6D). To understand whether Mtb utilizes hepatic lipid droplets as a source of nutrients in hepatocytes, we treated Mtb-infected hepatocytes with specific inhibitors of de-novo fatty acid biosynthesis (C75) and TAG biosynthesis (T863) (Fig 6E). Interestingly, inhibiting both de-novo fatty acid biosynthesis as well as TAG biosynthesis reduced the bacterial load in both PHCs and HepG2 by almost 1.0-1.5 log fold (Fig 6F and G). In THP-1 macrophage, although C75 reduced bacterial load by 0.5 log fold but

T863 did not affect the bacterial load (Fig- 6H). Our studies thus demonstrate fatty acid biosynthesis and TAG formation to be important for Mtb growth in hepatocytes.

**Systemic Mtb infection of mice via the aerosol route leads to significant infection of the liver and primary hepatocytes.**

Ex-vivo and in-vitro evidence of Mtb mediated changes in hepatocytes prompted us to study the involvement of liver in a murine aerosol Mtb infection model. We infected C57BL/6 mice with 200 CFU of Mtb H37Rv and scored for the bacterial load in the conventional niches like lungs and spleen as well as in the liver. Mtb disseminated to the liver consistently across several experiments in 4 weeks post-infection and the bacterial load increased till week 10 (Fig 7A). Consistent with the Mtb burden, phalloidin and hematoxylin and eosin (H and E) staining of the infected liver at 8 weeks post-infection showed localized aggregates of immune cells (CD 45.2 positive) forming a granuloma-like structure (Fig- 7C, S7 C, D). To assess whether liver infection leads to deranged liver function in the aerosol model, we analyzed the levels of liver functional enzymes like albumin aspartate transaminase (AST), alanine transaminase (ALT), and gamma-glutamyl transpeptidase (GGT) in the sera. Till week 10 post-infection, sera levels of these markers remain almost unchanged at the different time points post-infection (Fig S7B). Since hepatocytes, the principal parenchymal cells of the liver constitute 70-80 percent of the liver by weight, we hypothesized whether hepatocytes could harbor Mtb, in the mice model of infection. To this end, we isolated primary hepatocytes from the mice at different time points post-infection. The purity of the hepatocytes was validated microscopically by their distinct hexagonal architecture, round nucleus and by staining with asialoglycoprotein receptor (ASPGR) antibody (Fig S7 F). The isolated hepatocytes were

lysed and plated. Like the whole liver CFU, Mtb infected PHCs at 4 weeks post-infection with substantial bacterial load at week 6 and week 8 (Fig 7B). Antigen 85 (Ag85) staining in both the infected tissue sections and cultured hepatocytes revealed the presence of Mtb within hepatocytes (Fig 7D, E). Besides the aerosol route, infection intraperitoneally also led to hepatocyte infection, also led to hepatocyte infection as early as day 10 (Fig S7A). To assess the status of the neutral lipids in the liver, BODIPY staining was conducted in the liver cryosections of uninfected and infected mice (8 weeks post-infection). Liver of Mtb-infected mice bears more lipid bodies (Fig 7F). Co-immunostaining of BODIPY and Ag85B also indicated a certain degree of colocalization of Mtb and Lipid bodies in the liver (Fig S7E). Next, we stained the liver of Mtb infected mice at 2-, 4- and 8-weeks post infection with LipidTOX neutral red dye. Surprisingly we found an elevated signal intensity of the dye at 8 weeks post infection. This shows that in mice, Lipid droplets might correlate with Mtb burden (Fig S7G, H). Our data comprehensively establishes hepatocytes as a niche for Mtb during classical mouse aerosol infection model and established infection-induced steatosis as a pathogenic outcome of Mtb involvement in liver in the chronic stage of infection.

**PPARγ upregulation in Mtb-infected hepatocytes leads to augmented lipid biogenesis.**

To understand the molecular mechanism behind the accumulation of lipid droplets in the Mtb-infected liver at 8 weeks post-infection, we investigated the expression patterns of the transcription factors involved in the regulation of the genes of lipid biogenesis in our RNA-seq data. At 48 hours post-infection, the transcript levels of Peroxisome proliferator-activated receptor-gamma (PPARγ) were upregulated by 5-6-fold. To validate, that we

performed quantitative real-time PCR analysis of the *PPAR γ* gene in the infected HepG2 at 48 hours post-infection. With respect to the uninfected control, *PPAR γ* was upregulated by 3-4-fold. Besides, downstream adipogenic genes that are directly or indirectly controlled by *PPARγ* like *MGAT1*, *FSP27*, *FASN*, *DGAT1*, *DGAT2*, *ACAT1, ACAT2, ADIPSIN* etc were all upregulated by more than 2-fold in the infected cells (Fig S8 A). Immunoblot also revealed a greater level of PPARγ protein in primary mouse hepatocytes at 24 hours and 48 hours post infection in the Mtb infected cells (Fig 8C, D) .In the in-vivo Mtb aerosol infection model, *Pparγ* expression levels showed an intriguing trend, at week 2 post-infection, the expression level was comparable to the uninfected control, while at week 4 post-infection, the expression level spiked to 1.5-2-fold, reaching 3-4 fold at week 8 (Fig 8A). The pattern of expression of *Pparγ* in the infected liver correlated with the bacterial load in the liver, where we see the induction at week 4 when Mtb reaches the liver and maximum expression at week 8 when the load of Mtb is considerably high. Besides, PPARγ, some of the critical enzymes involved in fatty acid biosynthesis, TAG biosynthesis, cholesterol esterification like *Fasn, Dgat1, Dgat2, Mgat1, Acat1, Acat2* etc showed a temporal increase in expression levels at the later time points post-infection (Fig 8A). We then used a specific inhibitor of PPARγ, GW9662 (20 μM) and agonist of PPARγ, rosiglitazone (20μM) in infected HepG2 and quantified the bacterial load after 48 hours. Surprisingly, inhibition of PPARγ decreased the bacterial load by almost 2-fold, while chemically inducing PPARγ increased the bacterial load considerably. Moreover, LD number in cells also directly correlated with the levels of PPARγ (Fig 8E, F). To investigate whether, PPARγ expression was also induced in the liver of infected mice, we examined PPAR-γ in the liver post infection. Interestingly, we found enhanced expression PPARγ in

the liver of the mice at 8 weeks post infection (Fig S8 C, D). Moreover, PPAR-γ intensity in hepatoctyte was also high in the infected liver (Fig SF). Thus, PPARγ activation resulting in lipid droplets formation by Mtb might be a mechanism of prolonging survival within hepatocytes.

## Discussion

Mtb is recognized to infect multiple tissues and various cell types, however, our mechanistic understanding of Mtb biology is primarily derived from the macrophage infection models[35, 36]. Our studies here reveal hepatocytes as another predominant niche for Mtb survival and replication. We show that Mtb consistently colonizes hepatocyte 4 weeks post-infection in a classical murine-aerosol TB infection model. Considerably high bacterial load is observed during the week 6 to 8 (i.e., chronic phase of infection) and this colonization of hepatocytes results in two major consequential outcomes – (1). enhanced lipid biogenesis by upregulating PPARγ and (2) increased tolerance to isoniazid and rifampicin, by increasing the levels of the key DMEs. Evaluation of both these facets in the clinical setting, in future, can have significant impact on disease management.

Our studies demonstrate Mtb infection of hepatocytes surprisingly to be as efficient as the conventional phagocytes. Interestingly, despite the high bacterial load, infected hepatocytes showed no signs of cell death. At 24 hours post-infection, a major proportion of the tubercule bacilli resides within the early endosomal compartments, while a smaller portion could be found in the late endosomes within the hepatocytes. To obtain unbiased insights into the infection-induced gene expression changes in the hepatocytes, we

incubated Mtb with the hepatocytes for 5 hours and subsequently treated with amikacin to eliminate extracellular bacteria. The Mtb-enriched HepG2 cells were enriched and two time points of 0 hour (early) and 48 hours post-infection considered as a late stage for transcriptome analysis. Differential gene expression for early infection revealed upregulation of genes largely responsible for host defence. These include intracellular receptor signalling pathways, chromatin assembly, response to the xenobiotic stimulus, and response to reactive oxygen species. For the later time point, when the bacterial number has increased substantially, we observe key pathways like macroautophagy, regulation of lipid metabolism, fatty acid biosynthesis pathway, and proteasomal degradation pathway, to be significantly remodelled.

Our study here shows significant role for PPARγ-mediated enhanced expression of fatty acid biosynthetic genes and TAG biosynthetic genes. Mass spectrometric analysis of infected hepatocytes reveals increased levels of cholesterol esters (CE 16:0, 18:0, and 18:1), DAGS (36:1, 36:2, and 34:1), and TAGS (18:1/36:2, 18:0/ 36:2 and 18:0/ 36:1) with decreased levels of free cholesterol. This lipid remodelling of hepatocytes due to Mtb infection can be recapitulated in the murine aerosol model where we see an enhanced number of lipid droplets at week 8 with a localized accumulation of immune cells and granuloma-like structure. PPARγ up-regulates several proteins linked to lipid uptake, TAG storage, and lipid droplet providing credence that hepatic PPARγ expression promotes steatosis. By using agonist and antagonist of PPAR-γ, a corresponding decrease or increase in bacterial burden was observed thus highlighting the key role of PPARγ in Mtb survival in hepatocytes. Previous hepatocyte-specific deletion of the *Pparγ* gene reduced

liver steatosis in ob/ob mice, but adenovirus-mediated overexpression of PPARγ2 in hepatocytes increased hepatic steatosis[37, 38].

It is quite surprising that Mtb infection of hepatocytes has been largely ignored thus far. In a previous study discusses restricted transmission of Mtb Erdman and BCG strains to hepatocytes due to presence of resident macrophages. This discrepancy might be due to the time of harvesting of the organ post-infection[39]. In contrast, an interesting study recently revealed that *M. leprae* infection of the hepatocytes results in enhanced liver regeneration capacity in 9 banded armadillos, highlighting the effect of bacilli infection on hepatocyte biology[40]. Our human clinical analysis from autopsy findings shows ectopic granuloma-like structures in human liver biopsy samples with the presence of Ag85B signals within hepatocytes, emphasizing hepatocyte to be the new niche of Mtb survival.

Another important finding relates with the increased transcript levels of DMEs in the liver of mice after 8 weeks. The enhanced expression of DMEs is recapitulated, 48hours post-infection in hepatocytes resulting in development of drug tolerant bacteria. This aspect requires careful consideration in the context of human TB infection, particularly since many patients come to the clinic during chronic infectious phase[41, 42]. In the clinical scenario, such an activation of DMEs will alter pharmacokinetics and pharmacodynamics of anti-TB drugs resulting in sub-optimal drug concentrations and subsequent generation of drug-resistant strains[43].

Several recent publications directly correlate infection of hepatocytes with hyperglycaemia[44, 45] . With multiple reports correlating hepatic steatosis with the onset of Type 2 Diabetes Mellitus (T2DM), it can be hypothesized that TB-induced hepatic

steatosis might predispose TB patients to T2DM and other metabolic disorders. Considering all these clinically important parameters, it is important to target this metabolically privileged hepatocyte niche for better outcomes to multiple organ-wide derangements in TB pathogenesis.

**Acknowledgement**

We thank Dr. Lakshyaveer Singh, Tuberculosis Aerosol Challenge Facility (TACF), ICGEB for mice experiments. We thank Dr. Neerja Wadhwa for help in the NII Central Confocal facility, Mr.Birendra Kumar Roy for the preparation of the Cryosections and NII animal facility for providing us with the animals. We thank Next Generation Sequencing (NGS) facility at CSIR-CCMB for transcriptomic support. We are grateful to Science and Engineering Research Board for a Swarna Jayanti Fellowship to SSK (grant number: SB/SJF/2021-22/01) and a Department of Science and Technology Fund for Improvement of S&T Infrastructure (DST-FIST) (grant number SR/FST/LSII-043/2016) to the IISER Pune Biology Department for building a biological mass spectrometry facility. The Project is funded by NII core fund, Department of Biotechnology (DBT).

**Author Contribution**

BS and RSG conceptualized the study and analyzed the data. BS, DSG, JS, MY, PS, RDS performed the experiments. Human liver sections were stained by SS under the guidance from AK. Transcriptomic analysis was done by JS. Sorting was done by PS and RDS under the guidance from DK. Mass spectrometry analysis was conducted by AC under the supervision of SSK. BS and RSG wrote the manuscript. BS, DM, DSG, AK, SSK, DK and RSG reviewed and edited the manuscript. RSG supervised the project.

## Declaration of Interests

The authors declare no conflicts of interests.

## Materials and Methods

### Ethical clearances

**Human studies:**

Paraffinized non-Mtb infected, and Mtb-infected human autopsied liver specimens were obtained from the Postgraduate Institute of Medical Education and Research, Chandigarh, India. The Institutional Ethics Committee of CSIR-IMTech granted approval for all research experiments involving human samples (Approval no [IEC (May 2021) #6]). To ascertain the histological features of TB in these specimens, 5 µm thick tissue sections were prepared. These sections were then stained with H and E and examined under a microscope. Alternatively, these specimens were also used for FISH experiments.

**Animal studies:**

All the mice (C57BL/6) were housed in the animal house at the National Institute of Immunology (NII) before being transported to the TACF-ICGEB (Tuberculosis Aerosol Challenge Facility), for subsequent animal infection studies. The animal experiments were performed adhering to the institutional guidelines (Approval number: Institutional Animal Ethical Committee, IAEC 543/20.)

### Confocal microscopy and Immunofluorescence measurements:

Lipid droplets were stained by BODIPY 493/503 dye. Primary mouse hepatocytes and HepG2 cells were grown on 12 mm coverslips at respective densities as per the experimental requirement. Cells were washed with 1X PBS (HiMedia M1452-500G), fixed

by 4% paraformaldehyde, and incubated at room temperature for 15 minutes. After incubation, the cells were washed thrice with 1X PBS followed by staining with 10 μM BODIPY dye in 1XPBS for 45 minutes at room temperature. After the staining, the excess dye was removed by washing thrice with 1X PBS. To check for the acidified compartments within the cells, LysoTracker™ Red DND-99 (L7528) was added to the cells at a concentration of 500 nM for 30 minutes at 37$^{o}$ Celsius, followed by washing thrice with 1X PBS to remove the residual dye. The cells were fixed with 4% paraformaldehyde as previously mentioned. For staining with various antibodies, the cells were permeabilized with 0.2% Triton-x 100 (X-100-1L) for 15 minutes, followed by proper washing with 1X PBS. The cells were then blocked by 2% BSA in 1X PBST for 1 hour at room temperature. Post blocking, the cells were treated with primary antibody overnight at 4$^{o}$Celsius, followed by proper washing with 1X PBS. Secondary antibody (1:500 dilution) was added to the cells for 1 hour at room temperature. Three washes with 1X PBS were given. The nucleus was stained with DAPI (Sigma D9542-5MG) at 1ug/ml concentration for 20 minutes at room temperature. The excess DAPI was washed with 1X PBS followed by mounting with ProLong™ Gold Antifade mountant (P36930). Images were acquired by Zeiss LSM 980 Laser scanning confocal microscope.

**Image Analysis**

Analysis was done using Image J and Zen blue software. Mean fluorescent intensity/ cell was calculated by corrected total cell fluorescence (CTCF) = Integrated Density – (Area of Selected Cell x Mean Fluorescence of Background readings). Signal intensity in tissue sections were normalised to respective areas.

## Tissue Immunofluorescence staining

### Paraffin sections

Five-micron thick sections of paraffin-embedded tissue sections were taken in poly-L-Lysine coated slides (P0425-72EA). Deparaffinization was performed by heating the slides at 50$^{o}$C for 20 seconds (3 times) till the wax melts, followed by the subsequent steps, 100% xylene (Merck, CAS-1330-20-7) for 10 minutes (3 times), xylene and absolute ethanol (Merck, CAS- 64-17-5) for 10 minutes, 100% ethanol for 10 minutes, 70% percent ethanol for 5 minutes (2 times), 50% ethanol, distilled water for 5 minutes (2minutes) and a final wash in 1x PBS for 5 minutes (2 times). Antigen retrieval was performed in an antigen retrieval buffer (10mM Sodium Citrate, 0.05% tween-20, pH: 6) by heating the slides at 60$^{o}$C for 15 minutes. After antigen retrieval, permeabilization was performed with 0.4% Triton-X 100 in 1X PBS for 20 minutes followed by proper washing with 1x PBS. Blocking was done with 5% BSA for 1 hour. Sequential addition of primary antibody was performed at 1:100 dilution at 4$^{o}$C overnight. Primary antibody was washed with 1X PBS followed by counter stain with DAPI nuclear stain at 1 ug/ml concentration. Mounting was done with a drop of vectashield (sigma-aldrich, F6182-20ml). The slides were visualised in Zeis LSM 980 confocal microscopy at 40X (oil) magnification.

### Cryosections

Seven-micron thick cryosections were taken in poly-L-Lysine coated slides (P0425-72EA). The sections were washed with 1X PBS, 3 times for 5 mins each. Permeabilisation was done with 0.25% Triton-X 100 in 1X PBS for 15 minutes followed by washing with 1X PBS. Blocking was done with 5% BSA for 1 hour followed by incubation with primary antibody overnight at 4$^{o}$C. After that the slides were washed with 1X PBS 2 times for 5

minutes each followed by incubation with fluorophore conjugated secondary antibody for 45 minutes. The slides were washed with 1X PBS followed by counterstain with DAPI at 1ug/ml concentration. Mounting was done with a drop of Vectashield (Sigma-Aldrich, F6182-20ml). The dilution of the dyes and antibodies used in the staining are mentioned in the table.

For staining with BODIPY, the sections were incubated with 15 ums of BODIPY for 40 minutes at room temperature. The slides were visualized in Zeis LSM 980 confocal microscopy at 40X (oil) magnification.

**Fluorescence in-situ hybridization**

FISH was used to detect Mtb in infected human liver following published protocols (1-3). Briefly, the paraffinized human liver tissue sections were initially deparaffinized using a serial washing step with xylene and ethanol, following which the sections were treated with 1 mg/ml Proteinase K and 10 mg/ml Lysozyme in 10 mM Tris (pH 7.5) at 37°C for 30 min. Next, the samples were incubated in the Prehybridization buffer at 37°C for 1 h. Prehybridization buffer is composed of 20% 2X Saline sodium citrate (SSC), 20% Dextran sulfate, 30% Formamide, 1% 50X Denhardt's reagent, 2.5% of 10 mg/ml PolyA, 2.5% of 10 mg/ml salmon sperm DNA, 2.5% of 10 mg/ml tRNA. The slides were thoroughly washed with a 2X SSC buffer. The sections were then incubated in hybridization buffer at 95°C for 10 min and then chilled on ice for 10 min. Further hybridization was allowed at 37°C overnight. Hybridization buffer is composed of prehybridization buffer plus 16S Mtb-$H_{37}$ Rv probe (5′ FITC – CCACACCGCTAAAG – 3′), which is specific for the 16S rRNA of Mtb at a final concentration of 1 ng/µl. The liver tissue sections were next subjected to a series of washing steps with 1X SSC at room temperature for 1 min, 1X SSC at 55°C

for 15 min, 1X SSC at 55°C for 15 min, 0.5X SSC at 55°C for 15 min, 0.5X SSC at 55°C for 15 min, 0.5X SSC at room temperature for 10 min. Coverslips were mounted on glass slides and visualized using Nikon A1R confocal microscope with a 488 nm laser.

**Acid Fast Staining and Auramine O and Rhodamine B staining in liver sections.**

Acid-fast staining was performed using a ZN Acid Fast Stains-Kit (K005L-1KT, HIMEDIA). Prior to staining, the paraffinized samples were deparaffinized using a serial washing step with xylene and ethanol 1. 100% Xylene for 6 min, 2. Xylene: Ethanol 1:1 for 3 min, 3. 100% Ethanol for 3 min, 4. 95% Ethanol for 3 min, 5. 70% Ethanol for 3 min, 6. 50% Ethanol for 3 min, 7. Distilled water. The glass slides were flooded with Carbol Fuchsin stain and heated to steam for 5 min with a low flame. The glass slides were allowed to stand for 5 min without further heating. The glass slides were then washed in running tap water. The glass slides were decolorized with acid-fast decolourizer for 2 min. 5. Washed with tap water. 6. Counterstain for 30 sec with Methylene Blue Washed with tap water, dried in air, and examined under 100x objective with oil immersion. The presence or absence of bacteria in infected and uninfected samples was checked through staining with Phenolic Auramine O-Rhodamine B dye (4) (1/3 dilution of stock solution) (Auramine O-861020-25gm, Sigma) (Rhodamine B-R6626-100gm, Sigma). Coverslips were mounted on glass slides and visualized using CLSM with a 488 nm laser.

**Bacterial cultures and in-vitro experiments**

Virulent laboratory strains of H37Rv, BCG, and GFP-H37Rv bacterial cultures were cultivated on 7H9 medium (BD Difco) supplemented with 10% Albumin-Dextrose-Catalase (OADC, BD, Difco) for in vitro assays. The cultures were then incubated in an

orbital shaker at 100 rpm and 37 °C until the mid-log phase. pMN437-GFPm2 vector (Addgene, 32362) was used to electroporate the virulent H37Rv strain in order to create GFP-H37Rv, which was then maintained in 50 µg/ml hygromycin 7H9-OADC medium. pMSP12: mCherry plasmid (Addgene No. 30169) was electroporated in H37RV to generate Mtb-H37Rv-mCherry.To prepare the single-cell suspension needed for infection tests, bacterial cultures were passed through a sequence of different gauge needles five times through 23-gauge, 26-gauge, and three times through 30-gauge.

In-vitro and ex-vivo infection experiments in primary cells and different cell lines were performed at a Multiplicity of infection of 10 (MOI: 10) for both CFU enumeration and confocal microscopy. The macrophage experiments involving THP-1 and RAW 264.7 involved incubating the cells with Mtb-H37Rv for 5-6 hours followed by washing with 1X PBS and amikacin treatment (200 ug/ ml for 2 hours) to remove the extracellular bacteria. The cells were kept for the designated time points for 24 hours, 48 hours and so on and then lysed with lysis buffer (0.05 % SDS in 1X PBS) followed by plating in 7H11 plates.
For primary mouse hepatocytes and AML-12 cells, the cells were infected with the Mtb at a multiplicity of 10 for 8 hours followed by amikacin treatment (200 ug/ ml for 2 hours). For HepG2 and Huh-7, the time of incubation was 5- 6 hours followed by washing with 1X PBS and amikacin treatment as previously mentioned to remove the extracellular bacteria.

The percent drug tolerant population was calculated using the following formula (A/B X 100) where A is the CFU in the drug treated group, B is the CFU in the untreated group.

The cells were morphologically checked for signs of cell death before proceeding with the plating. For the inhibitor and inducer experiments, the cells were treated with the respective drugs for 48 hours post uptake of Mtb. After that they were lysed and Mtb CFU was enumerated.

**C57BL/6 aerosol challenge**

The mice infection experiments were conducted in the Tuberculosis Aerosol Challenge Facility (TACF, ICGEB, New Delhi, India). C57BL/6 mice were placed in individual ventilated cages within the enclosure, maintaining a temperature of 20-25$^{o}$C, 30-60 % humidity and 12h-12h of light-dark cycle. Following the standardized protocol, mice were infected with 200 CFUs of H37Rv in a Wisconsin-Madison chamber. To ensure proper establishment of infection, two animals were euthanized 24 hours post aerosol challenge. The lungs were harvested and homogenised in 1X PBS and plated in Middlebrook 7H11 agar plates (Difco) supplemented with 10% OADC and 0.5% glycerol. CFU enumeration was done three weeks post plating.

**C57BL/6 peritoneal infection**

The mice were injected with $10^6$ CFUs of H37Rv in 0.2 ml of 1X PBS. Following infection, on different days post infection, the lung, spleen, and the liver was harvested and homogenized and plated in Middlebrook 7H11 agar plates (Difco) supplemented with 10% OADC and 0.5% glycerol. CFU enumeration was done three weeks post plating.

**List of antibodies and dyes used in the study.**

| Serial number | Antibodies and dyes | Catalogue number | Company | Application and dilution |
|---|---|---|---|---|
| 1. | Rab5 | 2143T | CST | IF/ICC (1:200) |
| 2. | Rab7 | D9F2 | CST | IF/ICC (1:200) |
| 3. | Cathepsin D | Ab75852 | Abcam | IF/ICC (1:150) |
| 4. | LAMP1 | 9091T | CST | IF/ICC (1:200) |
| 5. | EEA1 | 3288T | CST | IF/ICC (1:200) |
| 6. | ASPGR1 | PA5-32030 | Invitrogen | IF/ICC (1:500) |
| 7. | PPAR γ | PA3-831A | Invitrogen | IF/ICC (1:150)<br>WB (1:1000) |
| 5. | Ag85B | Ab43019 | Abcam | IF/ICC (1:800) |
| 6 | CD45-APC (clone 104) | 558702 | BD biosciences | 1:300 |
| 7. | β-actin rabbit polyclonal Antibody. | 4967 | CST | IF/ICC (1:100)<br>WB (1:2000) |
| 8. | Goat anti-rabbit IgG (H+L) secondary Ab Alexa fluor 555 Plus | A32732 | Thermo fischer Scientific | IF/ICC (1:400) |
| 9. | Goat anti-rabbit IgG (H+L) Secondary Antibody, Alexa Fluor 488 | A11008 | Thermo fischer Scientific | IF/ICC (1:400) |
| 10. | Goat anti-rabbit IgG (H+L) Secondary Antibody, Alexa Fluor 405 | A-31556 | Thermo fischer Scientific | IF/ICC (1:400) |

| | | | | |
|---|---|---|---|---|
| 11. | Lysotracker Red | L7528 | Invitrogen | 500 nM |
| 12. | BODIPY-493/503 | D3922 | Invitrogen | Staining (10-15 µM) |
| 13. | Phalloidin-Alexa fluor 488 | A12379 | Invitrogen | IF/ICC 1 unit/slide |
| 14. | Phalloidin-Alexa Fluor 555 plus | A30106 | Invitrogen | IF/ICC 1 unit/slide |
| 15. | HCS LipidTOX™ Red Neutral Lipid Stain | H34476 | Invitrogen | IF/ICC (1:400) |
| 16. | DAPI | D9542 | Sigma-aldrich | 1 ug/ml |
| 17. | ZN Acid Fast Stains | K005L-1KT | Himedia | |
| 18. | Auramine O | 861020-25gm | Sigma-Aldrich | |
| 19 | Rhodamine B | R6626-100gm | Sigma-Aldrich | |

**List of reagents in the study**

| **Serial no** | **Reagents** | **Catalogue number** |
|---|---|---|
| 1. | C75 | C5490-5MG, Sigma-Aldrich |
| 2. | OA-BSA | O3008-5ML, Sigma-Aldrich |

| | | |
|---|---|---|
| 5. | GW9662 | M6191-25MG, Sigma-Aldrich |
| 6. | Rosiglitazone | R2408-10MG, Sigma-Aldrich |
| 7. | T863 | SML0539-5MG, Sigma-Aldrich |
| 8. | Rifampicin | 557303-1G, Merck |
| 9. | Isoniazid | I3377-5G, Merck |

**Sorting of labelled H37Rv cells**

The infected hepatocytes were trypsined and washed with 1X PBS followed by passing through 40µm cell strainer to make single cell suspension. After that the cells positive for mCherry signals were sorted using the BD FACS Aria at TACF, ICGEB. Approximately 1 million cells were used for RNA isolation per sample.

**Primary hepatocyte Isolation**

After euthanizing the mice, the peritoneal cavity was opened, and the liver was perfused with 1X HBSS solution till exsanguination was complete. After that collagenase solution (17 mg in 30 ml of 1X HBSS) was passed for digestion. The liver was cut into small pieces and kept in 25 ml of DMEM media followed by lysing the tissues with a glass pestle and sieve. The cells were then passed through a 70 µM cell strainer. 25 ml of percoll was added to the cells with proper mixing. It was centrifuged at 1000 rpm for 5 minutes. The floating cells were removed, and a brownish layer of pure hepatocytes pelted at the bottom. The cells were counted and plated according to the experimental need on a collagen coated plate.

**Lipid Extraction protocol and Mass spectrometry**

5 million HepG2 cells were infected with Mtb-H37Rv at MOI 10 and kept for 24 hours and 48 hours post-infection. An equal number of uninfected cells were taken. The cells were scrapped, and the procedure of Bligh and Dyer was followed[46]. In brief, the cells were lysed in 1% Triton X-100 after being rinsed twice with 1X PBS. Following lysis, the lysate was vortexed and four volumes of methanol-chloroform (2:1) were added. After that, one volume each of water, chloroform, and 50 mM citric acid was added and vortexed. Following a 10-minute centrifugation at 10,000 rpm at $4^{o}$ Celsius, the lower organic phase was collected and dried using liquid nitrogen. All semi-quantitative lipid measurements were done using previously reported high-resolution MS/MS methods and chromatographic techniques on an Agilent 6545 QTOF instrument. All sterols were resolved using a Gemini 5U C-18 column (Phenomenex) while DAGs/TAGs were resolved using a Luna 5U C-5 column (Phenomenex) using established solvent systems.

**Cell lysate preparation and Western blotting**

The cells were washed twice with 1X PBS followed by lysis with SDS-RIPA buffer (50 mM Tris-HCl pH 7.5, 150 mM NaCl, 1 mM EDTA, 0.1% SDS, 1% Triton-X 100, 1 mM DTT, 1X Proteinase inhibitor). The cells were incubated with the buffer for 30 minutes in ice followed by vortexing for 5 minutes. The supernantant fraction was collected by centrifuging at 10000 rpm for 20 minutes at $4^{O}$C. The protein concentration was determined by bicinchoninic acid (BCA) protein estimation kit (Thermo Fisher Scientific, Waltham, Massachusetts, USA, 23227) following the manufacturer's protocol. 60-80 ug of protein was resolved in SDS-PAGE followed by transferring onto a PVDF membrane. Blocking was done in 5% skimmed milk in 1X TBST followed by incubation with primary

antibodies overnight at 4$^{o}$C. The membranes were washed 3 times with 1x TBST for 10 minutes each followed by incubation with the HRP-conjugated secondary antibody for 1 hour. Immobilon HRP substrate was used to develop the blots and ImageQuant Chemiluminescent imaging system (LAS 500) was used to acquire the images. Band intensities were measured by using ImageJ.

**Gene expression studies**

**RNA isolation**

Total RNA was isolated from HepG2, PHCs and liver sections using the MN-NucleoSpin RNA isolation kit (740955.250) following the manufacturer's protocol. For RNA sequencing, an equal number of cells was used during isolation. For Liver tissue, approximately 10mg was tissue was used. The quality of the RNA was verified by running it on a 1.5% agarose gel and by monitoring 260/280 ratios. All the RNA samples were frozen together in -80$^{o}$C. For RNA sequencing, 3-5 ug of RNA was shipped in sodium acetate buffer (3 M Sodium acetate, pH 5.2) with 100% Ethanol. 4 biological replicates from each time point were sent for sequencing. The RNA samples with RNA integrity number (RIN > 8.5) were used for library preparation.

RNA samples (for four biological replicates) were subjected to pair-end RNA sequencing after rRNA depletion on the Illumina platform Novaseq-6000 at CCMB, Hyderabad, India. Quality control and sequence trimming was performed using fastp (v0.23.2). The trimmed paired-end reads were aligned to the human genome (GRCh38) using the HISAT2 (v2.2.1) pipeline. Reads were assembled into transcripts using StringTie (v2.2.1). Annotation was conducted using aligned sequences and a GTF annotation file. The

mapped reads were then used for generating the count table using StringTie (v2.2.1), genes lacking an Ensembl ID annotation were excluded. We arrived at a list of 62694 genes which were used for further analysis (available through GEO accession-GSExxxxxx). The differential count was performed by DEseq2 (R package) using the uninfected samples of respective time points. Pathway enrichment was performed using the GO database and clusters were visualized using the R package ClusterProfiler. Further pathways of interest were analysed by GAGE and visualized using Pathview in KEGG view.

**cDNA synthesis and RT-qPCR**

1ug of RNA was reverse transcribed to cDNA using the Takara cDNA synthesis kit (6110A) as per the manufacturer's protocol. Gene expression analysis by quantitative real-time PCR was performed PowerUp SYBR Green PCR (Thermo fischer scientific, (A25742) master mix in ABI 7500 FAST instrument. Beta-actin was used as the normalizing control and comparative Ct method was used for quantification.

**List of primers used in the study.**

| GENE NAME | FORWARD PRIMER (5'---------->3') | REVERSE PRIMER (5'---------->3') | SPECIES |
|---|---|---|---|
| β-actin | ATGGAGGGGAATACAGCCC | TTCTTTGCAGCTCCTTCGTT | Mouse |
| ppar-γ | CTCTGGGAGATTCTCCTGTTGA | GGTGGGCCAGAATGGCATCT | Mouse |
| ppar-α | AGAGCCCCATCTGTCCTCTC | ACTGGTAGTCTGCAAAACCAAA | Mouse |
| fasn | CTGCGTGGCTATGATTATGG | AGGTTGCTGTCGTCTGTAGT | Mouse |
| acat1 | CAGGAAGTAAGATGCCTGGAAC | TTCACCCCCTTGGATGACATT | Mouse |
| acat2 | CCCGTGGTCATCGTCTCAG | GGACAGGGCACCATTGAAGG | Mouse |
| dgat1 | TGCCCTGACAGAGCAGATGG | CAGGTTGACATCCCGGTAGG | Mouse |
| dgat2 | TGGCGCTACTTCCGAGACTAC | TGCTGACTTCAGTAGCCTCTGTG | Mouse |

| | | | |
|---|---|---|---|
| nat2 | ACACTCCAGCCAATAAGTACAGC | GGTAGGAACGTCCAAACCCA | Mouse |
| Slco1b2 | GGGAACATGCTTCGTGGGATA | GGAGTTATGCGGACACTTCTC | Mouse |
| aadac | TACCGCTTCCAGATGCTATTGA | ACTGATTCCCAAAAGTTCACCAA | Mouse |
| cyp2e1 | CATCACCGTTGCCTTGCTTG | GGGGCAGGTTCCAACTTCT | Mouse |
| ces1c | GCACTACGCTGGGTCCAAGAT | AAAGATGGTCACGGAATCCG | Mouse |
| ces2c | GCTGAATGCTGGGTTCTTCG | GCTGCCTTGGATCTGTCCTGT | Mouse |
| β-actin | AAGGCCAACCGCGAGAAGAT | GCCAGAGGCGTACAGGGATA | Human |
| pparγ | GGTGAAACTCTGGGAGATTCT | CTCTGTGTCAACCATGGTCA | Human |
| fasn | AGTACACACCCAAGGCCAAG | GTGGATGATGCTGATGATGG | Human |
| acat1 | TACCAGAAGTAAAGCAGCATGG | TCATTCAGTGTACTGGCATTGG | Human |
| acat2 | CTTTAGCACGGATAGTTTCCTGG | GCTGCAAAGGCTTCATTGATTTC | Human |
| dgat1 | CAATCTGACCTACCGCGATCT | TCGATGATGCGTGAGTAGTCC | Human |
| dgat2 | GAATGGGAGTGGCAATGCTAT | CCTCGAAGATCACCTGCTTGT | Human |
| nat2 | CCAGAAGGGGTTTACTGTTTGG | CAGGTTTGGGCACGAGATTTC | Human |
| mgat1 | CGCAAGTTCCAGGGCTACTAC | CTTCAGCAGCGGATAGGTGG | Human |
| fsp27 | ATGGACTACGCCATGAAGTCT | CGGTGCTAACACGACAGGG | Human |

## List of reagents in the study

| **Reagent** | **Company** | **Catalogue number** |
|---|---|---|
| Immobilon Forte Western HRP substrate | Millipore | WBLUF0500 |
| Amersham™ Hybond® P Western blotting membranes, PVDF | Merck | GE10600023 |

| | | |
|---|---|---|
| PowerUP SYBR | Thermo Fischer Scientific | A25742 |
| Vectashield | Sigma-Aldrich | F6182 |
| Primescript 1st strand cDNA synthesis kit | Takara Bio | 6110A |
| NucleoSpin RNA isolation Kit | Macherey-Nagel | 74106 |
| ProLong™ Gold antifade reagent | Thermo Fischer Scientific | P36930 |
| PolyFreeze Tissue Freezing medium | Sigma- Aldrich | SHH0026 |
| Microscope slides | Himedia | BG005 |
| Poly-Prep slides | Sigma- Aldrich | P0425-72EA |

## References


1. *Global Tuberculosis Report* 2023, World Health Organisation (WHO).

2. Seung, K.J., S. Keshavjee, and M.L. Rich, *Multidrug-Resistant Tuberculosis and Extensively Drug-Resistant Tuberculosis.* Cold Spring Harb Perspect Med, 2015. **5**(9): p. a017863.
3. Husain, A.A., et al., *Current perspective in tuberculosis vaccine development for high TB endemic regions.* Tuberculosis (Edinb), 2016. **98**: p. 149-58.
4. Eckhardt, M., et al., *A systems approach to infectious disease.* Nat Rev Genet, 2020. **21**(6): p. 339-354.
5. Davis, H.E., et al., *Long COVID: major findings, mechanisms and recommendations.* Nat Rev Microbiol, 2023. **21**(3): p. 133-146.
6. Lippi, G., F. Sanchis-Gomar, and B.M. Henry, *COVID-19 and its long-term sequelae: what do we know in 2023?* Pol Arch Intern Med, 2023. **133**(4).
7. Luies, L. and I. du Preez, *The Echo of Pulmonary Tuberculosis: Mechanisms of Clinical Symptoms and Other Disease-Induced Systemic Complications.* Clin Microbiol Rev, 2020. **33**(4).
8. Loddenkemper, R., M. Lipman, and A. Zumla, *Clinical Aspects of Adult Tuberculosis.* Cold Spring Harb Perspect Med, 2015. **6**(1): p. a017848.
9. Morley, J.E., D.R. Thomas, and M.M. Wilson, *Cachexia: pathophysiology and clinical relevance.* Am J Clin Nutr, 2006. **83**(4): p. 735-43.
10. Chang, S.W., et al., *Gut hormones, appetite suppression and cachexia in patients with pulmonary TB.* PLoS One, 2013. **8**(1): p. e54564.
11. Bisht, M.K., et al., *The cause-effect relation of tuberculosis on incidence of diabetes mellitus.* Front Cell Infect Microbiol, 2023. **13**: p. 1134036.
12. Niazi, A.K. and S. Kalra, *Diabetes and tuberculosis: a review of the role of optimal glycemic control.* J Diabetes Metab Disord, 2012. **11**(1): p. 28.

13. Jensen-Cody, S.O. and M.J. Potthoff, *Hepatokines and metabolism: Deciphering communication from the liver.* Mol Metab, 2021. **44**: p. 101138.
14. Kumar, N.P., et al., *Acute Phase Proteins Are Baseline Predictors of Tuberculosis Treatment Failure.* Front Immunol, 2021. **12**: p. 731878.
15. Quinton, L.J., A.J. Walkey, and J.P. Mizgerd, *Integrative Physiology of Pneumonia.* Physiol Rev, 2018. **98**(3): p. 1417-1464.
16. Shim, D., H. Kim, and S.J. Shin, *Mycobacterium tuberculosis Infection-Driven Foamy Macrophages and Their Implications in Tuberculosis Control as Targets for Host-Directed Therapy.* Front Immunol, 2020. **11**: p. 910.
17. Park, J.H., et al., *Understanding Metabolic Regulation Between Host and Pathogens: New Opportunities for the Development of Improved Therapeutic Strategies Against Mycobacterium tuberculosis Infection.* Front Cell Infect Microbiol, 2021. **11**: p. 635335.
18. Zhou, Z., M.J. Xu, and B. Gao, *Hepatocytes: a key cell type for innate immunity.* Cell Mol Immunol, 2016. **13**(3): p. 301-15.
19. Alper, C.A., et al., *Human C'3: evidence for the liver as the primary site of synthesis.* Science, 1969. **163**(3864): p. 286-8.
20. Wang, F., et al., *Organ-organ communication: The liver's perspective.* Theranostics, 2021. **11**(7): p. 3317-3330.
21. Silvie, O., et al., *Hepatocyte CD81 is required for Plasmodium falciparum and Plasmodium yoelii sporozoite infectivity.* Nat Med, 2003. **9**(1): p. 93-6.
22. Vaughan, A.M. and S.H.I. Kappe, *Malaria Parasite Liver Infection and Exoerythrocytic Biology.* Cold Spring Harb Perspect Med, 2017. **7**(6).
23. Protzer, U., M.K. Maini, and P.A. Knolle, *Living in the liver: hepatic infections.* Nat Rev Immunol, 2012. **12**(3): p. 201-13.
24. Tallan, A. and Z. Feng, *Virus spread in the liver: mechanisms, commonalities, and unanswered questions.* Future Virol, 2020. **15**(10): p. 707-715.
25. Meylan, S., I.W. Andrews, and J.J. Collins, *Targeting Antibiotic Tolerance, Pathogen by Pathogen.* Cell, 2018. **172**(6): p. 1228-1238.
26. Wu, Z., et al., *Diagnosis and treatment of hepatic tuberculosis: report of five cases and review of literature.* Int J Clin Exp Med, 2013. **6**(9): p. 845-50.
27. Turhan, N., et al., *Hepatic granulomas: a clinicopathologic analysis of 86 cases.* Pathol Res Pract, 2011. **207**(6): p. 359-65.
28. Sachdeva, K., et al., *Mycobacterium tuberculosis (Mtb) lipid mediated lysosomal rewiring in infected macrophages modulates intracellular Mtb trafficking and survival.* J Biol Chem, 2020. **295**(27): p. 9192-9210.
29. Day, N.J., P. Santucci, and M.G. Gutierrez, *Host cell environments and antibiotic efficacy in tuberculosis.* Trends Microbiol, 2023.
30. Ahmed, S., et al., *Pharmacogenomics of Drug Metabolizing Enzymes and Transporters: Relevance to Precision Medicine.* Genomics Proteomics Bioinformatics, 2016. **14**(5): p. 298-313.
31. Almazroo, O.A., M.K. Miah, and R. Venkataramanan, *Drug Metabolism in the Liver.* Clin Liver Dis, 2017. **21**(1): p. 1-20.
32. Yamashita, F., et al., *Modeling of rifampicin-induced CYP3A4 activation dynamics for the prediction of clinical drug-drug interactions from in vitro data.* PLoS One, 2013. **8**(9): p. e70330.
33. Sotsuka, T., et al., *Association of isoniazid-metabolizing enzyme genotypes and isoniazid-induced hepatotoxicity in tuberculosis patients.* In Vivo, 2011. **25**(5): p. 803-12.
34. Peyron, P., et al., *Foamy macrophages from tuberculous patients' granulomas constitute a nutrient-rich reservoir for M. tuberculosis persistence.* PLoS Pathog, 2008. **4**(11): p. e1000204.

35. Cosma, C.L., D.R. Sherman, and L. Ramakrishnan, *The secret lives of the pathogenic mycobacteria.* Annu Rev Microbiol, 2003. **57**: p. 641-76.
36. Bussi, C. and M.G. Gutierrez, *Mycobacterium tuberculosis infection of host cells in space and time.* FEMS Microbiol Rev, 2019. **43**(4): p. 341-361.
37. Lee, Y.K., et al., *Hepatic lipid homeostasis by peroxisome proliferator-activated receptor gamma 2.* Liver Res, 2018. **2**(4): p. 209-215.
38. Berthier, A., et al., *PPARs in liver physiology.* Biochim Biophys Acta Mol Basis Dis, 2021. **1867**(5): p. 166097.
39. Seiler, P., et al., *Limited mycobacterial infection of the liver as a consequence of its microanatomical structure causing restriction of mycobacterial growth to professional phagocytes.* Infect Immun, 2001. **69**(12): p. 7922-6.
40. Hess, S., et al., *In vivo partial reprogramming by bacteria promotes adult liver organ growth without fibrosis and tumorigenesis.* Cell Rep Med, 2022. **3**(11): p. 100820.
41. Ayalew, Y.E., et al., *Delay for Tuberculosis Treatment and Its Predictors among Adult Tuberculosis Patients at Debremarkos Town Public Health Facilities, North West Ethiopia.* Tuberc Res Treat, 2020. **2020**: p. 1901890.
42. Alavi, S.M., P. Bakhtiyariniya, and A. Albagi, *Factors associated with delay in diagnosis and treatment of pulmonary tuberculosis.* Jundishapur J Microbiol, 2015. **8**(3): p. e19238.
43. Dookie, N., et al., *Evolution of drug resistance in Mycobacterium tuberculosis: a review on the molecular determinants of resistance and implications for personalized care.* J Antimicrob Chemother, 2018. **73**(5): p. 1138-1151.
44. Barreto, E.A., et al., *COVID-19-related hyperglycemia is associated with infection of hepatocytes and stimulation of gluconeogenesis.* Proc Natl Acad Sci U S A, 2023. **120**(21): p. e2217119120.
45. Mercado-Gomez, M., et al., *The spike of SARS-CoV-2 promotes metabolic rewiring in hepatocytes.* Commun Biol, 2022. **5**(1): p. 827.
46. Bligh, E.G. and W.J. Dyer, *A rapid method of total lipid extraction and purification.* Can J Biochem Physiol, 1959. **37**(8): p. 911-7.

## Figure legend

**Figure 1: Presence of Mtb in human pulmonary tuberculosis patients: (A)** Hematoxylin and eosin (H and E) staining of the human autopsied liver tissue sections showing the presence of granuloma-like structure in the Mtb infected liver. **(B)** Acid-fast staining showing the presence of Mtb in the liver section of pulmonary TB patients. (yellow arrows point the presence of Mtb in the image) **(C-D)** Auramine O-Rhodamine B (A-O) staining and fluorescence in-situ hybridization (FISH) with Mtb specific 16s rRNA primer

further confirms the presence of Mtb in human liver tissue sections. Data shown here is a representative of 5 autopsied specimens having Mtb infection.

**Figure 2: Primary mouse hepatocytes and different hepatic cell lines support Mtb-*H37Rv* growth: (A and B)** Representative microscopic images showing the infection of Primary hepatocytes (PHCs), AML-12, HepG2, and Huh-7 with labelled Mtb-*H37Rv* strains and subsequent quantification of percentage infectivity in the respective cell types. RAW 264.7 and THP-1 macrophages are used as positive controls. The scale bar in all images is 10 µm except in HepG2, which is 5 µm **(C)** CFU enumeration of Mtb-*H37Rv* in different hepatic cell lines. **(D and E)** Representative confocal microscopy images of Mtb-GFP-*H37Rv* infected PHCs at the respective time points post-infection and bar blot depicting mean fluorescent intensity (MFI)/ cell at the respective time points. **(F and G)** Representative confocal microscopy images of Mtb-*H37Rv*-GFP infected HepG2 at the respective time points post-infection and bar blot depicting MFI/cell at the respective time points, n= 4 independent experiments, with each dot representing 5 fields of 30-60 cells. Scale bar 10 µm. Growth kinetics of Mtb-*H37Rv* in **(H)** HepG2 **(I)** PHCs **(J)** RAW 264.7 and **(K)** THP-1 at the respective time points post-infection.

**Figure 3: RNA sequence analysis of infected and sorted hepatocytes at 0 hours and 48 hours post-infection (A)** Experimental setup for infection of HepG2 with Mb-*H37Rv*-mCherry at 10 MOI with histogram of mCherry signals at 0- and 48-hours post-infection **(B)** Principal component analysis (PCA) plot illustrating the HepG2 transcriptome, identified through global transcriptomic analysis of 0 hours uninfected and infected and 48 hours uninfected and infected. **(C)** GO pathway enrichment analysis was

done for DEGs with adjusted p-value < 0.05 at 0- and 48-hours post-infection. The bubble plot depicts the enrichment of pathways on the mentioned time points post-infection, where the coordinate on the x-axis represents the gene ratio, the bubble size represents the gene count and colour represents the p-value. **(D and E)** Volcano plot depicting the fold change of different genes in 0 hours and 48 hours post-infection, the red dots represent the significantly upregulated and downregulated genes.

**Figure 4: Subcellular localization of Mtb-GFP-*H37Rv* within primary hepatocytes (PHCs) (A)** Representative microscopic images of colocalization of Mtb-*H37Rv*-GFP within various endosomal compartments (early-Rab5 and EEA1) and late (Cat D, Rab7, LysoRED+Cat D, LysoRED+RAb7 and LysoRED+LAMP1) in PHCs **(B)** Bar graph depicting the percentage of colocalization of Mtb-*H37Rv*-GFP with the above mentioned markers in HepG2, PHCs and THP-1 cells. Representative data from 50-70 cells, across 4 independent experiments. 2-way ANOVA was performed for the analysis of the colocalization data (Turkey's multiple comparison test) *p < 0.05, **p < 0.005, ***p < 0.0005, ****p < 0.0001, ns=non-significant.

**Figure 5: Hepatocytes provide a drug-tolerant niche to Mtb (A)** Experimental scheme of deducting the percentage drug tolerance in hepatocytes **(B)** Percentage tolerance of Mtb-*H37Rv* against Rifampicin within RAW 264.7, PHCs and HepG2 at different time points post-infection. **(C)** Percentage tolerance of Mtb-H37Rv against Isoniazid within RAW 264.7, PHCs, and HepG2 at different time points post-infection. Representative data from 3 independent experiments. 2-way ANOVA was performed for the analysis percentage tolerance data (Turkey's multiple comparison test) *p < 0.05, **p < 0.005, ***p

< 0.0005, ****p < 0.0001, ns=non-significant **(D)** Transcript levels of the various DMEs involved in Rifampicin and Isoniazid metabolism in mice liver, 8 weeks post-infection (n=4 mice), , the fold change has been calculated by considering the expression in the uninfected mice to be 1. Data were analysed by using by one-way ANOVA in (B) and (C) and the two tailed unpaired Student's t-test in (D) and Representative data from n=4 biological replicates *p < 0.05, **p < 0.005, ***p < 0.0005, ****p < 0. 0001.ns=non-significant.

**figure 6**: **Increased fatty acid biogenesis drives Mtb growth in hepatocytes**: **(A)** Increased number of LDs/cell in HepG2 and PHCs post-Mtb infection **(B)** Quantification of the number of lipid droplets in the infected HepG2 and PHCs with their uninfected control, 50-70 cells were analyzed from 3 independent experiments. **(C)** Increase in the BODIPY intensity at different days post-infection in infected hepatocytes **(D)** Mass spectrometric quantification of the different species of DAGs, TAGs and cholesterol esters in the Mtb infected hepatocytes. **(E)** Confocal microscopy showing the LDs in both PHCs and HepG2 under different inhibitors of fatty acid biosynthesis and TAG biosynthesis Relative CFU of Mtb under the administration of different inhibitors of the fatty acid biosynthetic pathway in **(F)** PHCs **(G)** HepG2 and **(H)** THP-1. Representative data from 3 independent experiments. Data were analysed using the two-tailed unpaired Student's t-test in B and one-way ANOVA in C, F, G, and H.*p < 0.05, **p < 0.005, ***p < 0.0005, ****p < 0.0001. ns=non-significant.

**Figure 7: Involvement of the liver and hepatocytes in a mouse aerosol model of Mtb infection**. **(A)** C57BL/6 mice were infected with 200 CFU of H37Rv through the aerosol route and the bacterial burden of the lungs, liver and spleen was enumerated at different time points post infection. (**B)** Primary hepatocytes were isolated from the infected mice, lysed and CFU enumeration was done at the mentioned time points. (**C)** Alexa Fluor TM 488 Phalloidin and DAPI staining of uninfected and infected lungs at 8 weeks post-infection. Images were taken in 20X, and 40 X magnification as mentioned (scale bar is 20 μm). (**D)** Immunofluorescence staining of Alexa Fluor TM 488 Phalloidin, DAPI, and Ag85B in the infected mice liver at 8 weeks post-infection shows the presence of Ag85B signals within hepatocytes (magnified image) (scale bar is 20 μm). **(E)** Ag85B staining of cultured primary hepatocytes, isolated from mice at 8 weeks post Mtb infection. (scale bar is 20 μm). **(F)** . BODIPY intensity of uninfected and infected mice at 8 weeks post-infection showing greater number of LDs in infected liver. Sample size (n)= 6-7 mice in each group.

**Figure 8: PPARγ driven lipid biogenesis drives Mtb growth in hepatocytes: (A)** Heat map showing the fold change of the genes involved in the lipid biosynthesis and LD biogenesis in liver across weeks 2, 4 and 8, post infection. **(B)** Kinetic increase in the gene expression of *Pparγ* transcript levels across different weeks post infection **(C)** Immunoblot showing increased PPARγ in PHCs (MOI: 10) at 5 ,24 and 48 hours post-infection. **(D)** Bar plot showing the increased band intensity of PPARγ in the infected PHCs at the mentioned time points. **(E)** Representative confocal microscopy images

showing HepG2 infected with Mtb-mCherry-*H37Rv* and treated with GW9662 and rosiglitazone **(F)** MFI/cell of in Mtb-mCherry-*H37Rv* DMSO treated, GW9662 and rosiglitazone treated HepG2 cells. **(G)** Representative confocal images of uninfected, infected, GW9662 and rosiglitazone treated infected HepG2 showing changes in the number of LDs. **(H)** Plot depicting the quantification of LDs/cell in the mentioned conditions. Representative data from n=4 biological replicates. Data were analysed by using the two tailed unpaired Student's t test in D and by one way ANOVA in B, F and H. *$p < 0.05$, **$p < 0.005$, ***$p < 0.0005$, ****$p < 0.0001$, ns=non-significant.

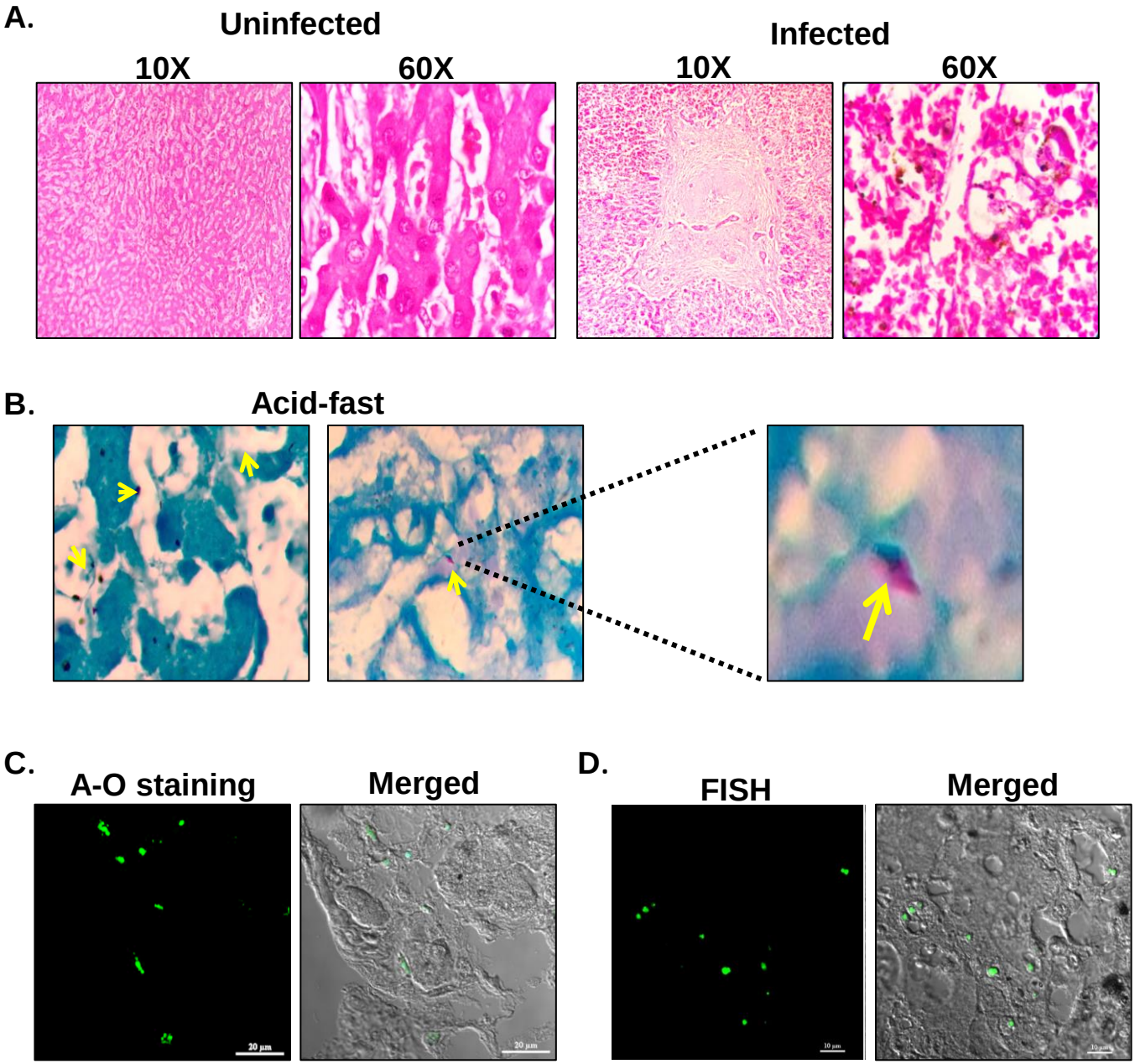
A.
Uninfected
10X
60X
Infected
10X
60X
B.
Acid-fast
C.
A-O staining
Merged
20 µm
20 µm
D.
FISH
Merged
10 µm
10 µm

Figure 1

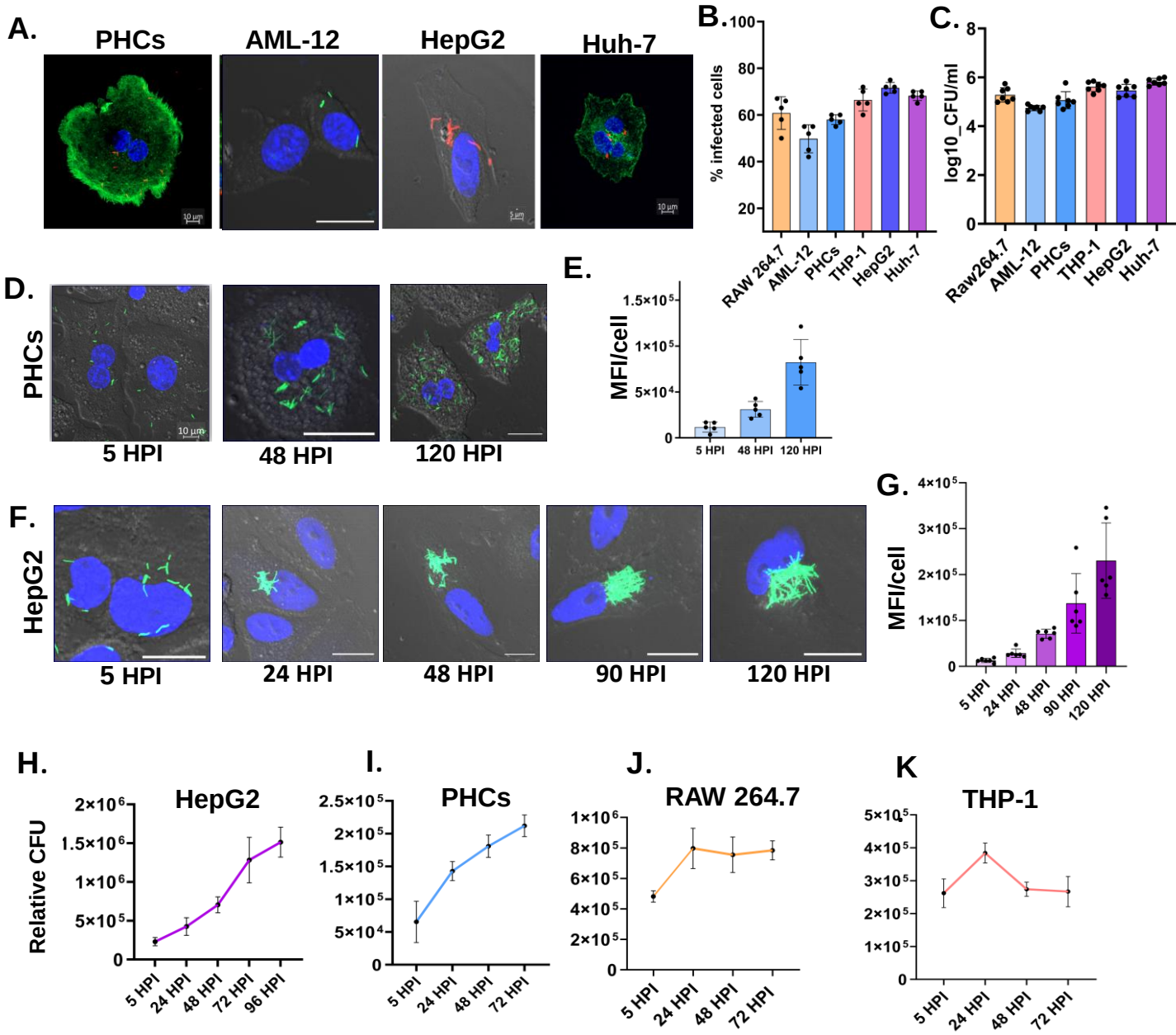
A.
PHCs
AML-12
HepG2
Huh-7
B.
% infected cells
100
80
60
40
20
RAW 264.7
AML-12
PHCs
THP-1
HepG2
Huh-7
C.
log10_CFU/ml
8
6
4
2
0
Raw264.7
AML-12
PHCs
THP-1
HepG2
Huh-7
D.
PHCs
5 HPI
48 HPI
120 HPI
E.
MFI/cell
1.5×10⁵
1×10⁵
5×10⁴
0
5 HPI
48 HPI
120 HPI
F.
HepG2
5 HPI
24 HPI
48 HPI
90 HPI
120 HPI
G.
MFI/cell
4×10⁵
3×10⁵
2×10⁵
1×10⁵
0
5 HPI
24 HPI
48 HPI
90 HPI
120 HPI
H.
HepG2
Relative CFU
2×10⁶
1.5×10⁶
1×10⁶
5×10⁵
0
5 HPI
24 HPI
48 HPI
72 HPI
96 HPI
I.
PHCs
2.5×10⁵
2×10⁵
1.5×10⁵
1×10⁵
5×10⁴
0
5 HPI
24 HPI
48 HPI
72 HPI
J.
RAW 264.7
1×10⁶
8×10⁵
6×10⁵
4×10⁵
2×10⁵
0
5 HPI
24 HPI
48 HPI
72 HPI
K
THP-1
5×10⁵
4×10⁵
3×10⁵
2×10⁵
1×10⁵
0
5 HPI
24 HPI
48 HPI
72 HPI

**Figure 2**

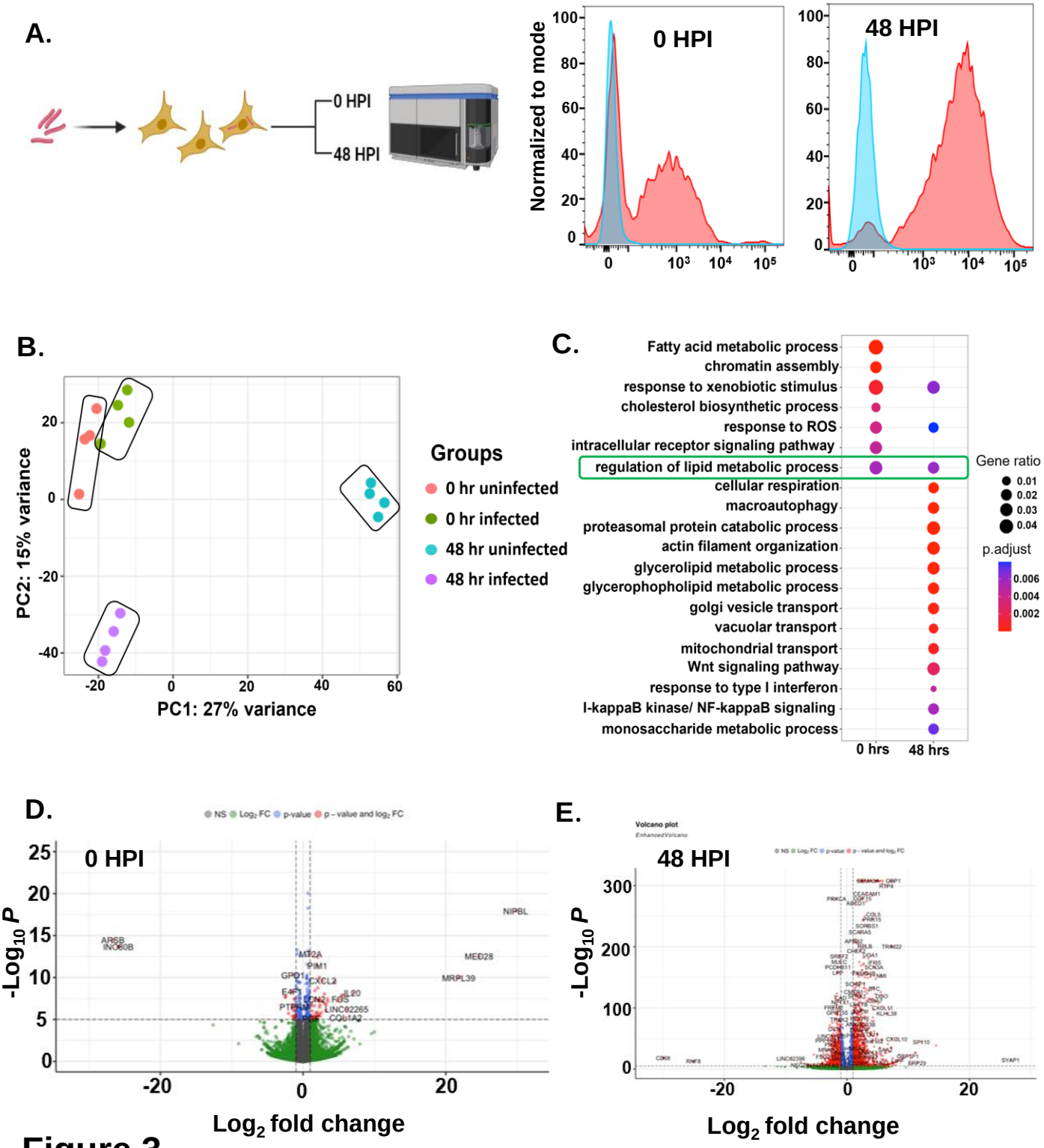
A.
0 HPI
48 HPI
Normalized to mode
0 HPI
48 HPI
B.
PC2: 15% variance
PC1: 27% variance
Groups
0 hr uninfected
0 hr infected
48 hr uninfected
48 hr infected
C.
Fatty acid metabolic process
chromatin assembly
response to xenobiotic stimulus
cholesterol biosynthetic process
response to ROS
intracellular receptor signaling pathway
regulation of lipid metabolic process
cellular respiration
macroautophagy
proteasomal protein catabolic process
actin filament organization
glycerolipid metabolic process
glycerophopholipid metabolic process
golgi vesicle transport
vacuolar transport
mitochondrial transport
Wnt signaling pathway
response to type I interferon
I-kappaB kinase/ NF-kappaB signaling
monosaccharide metabolic process
0 hrs
48 hrs
Gene ratio
0.01
0.02
0.03
0.04
p.adjust
0.006
0.004
0.002
D.
0 HPI
-Log10 P
Log2 fold change
NIPBL
MED28
MRPL39
E.
Volcano plot
48 HPI
-Log10 P
Log2 fold change

Figure 3

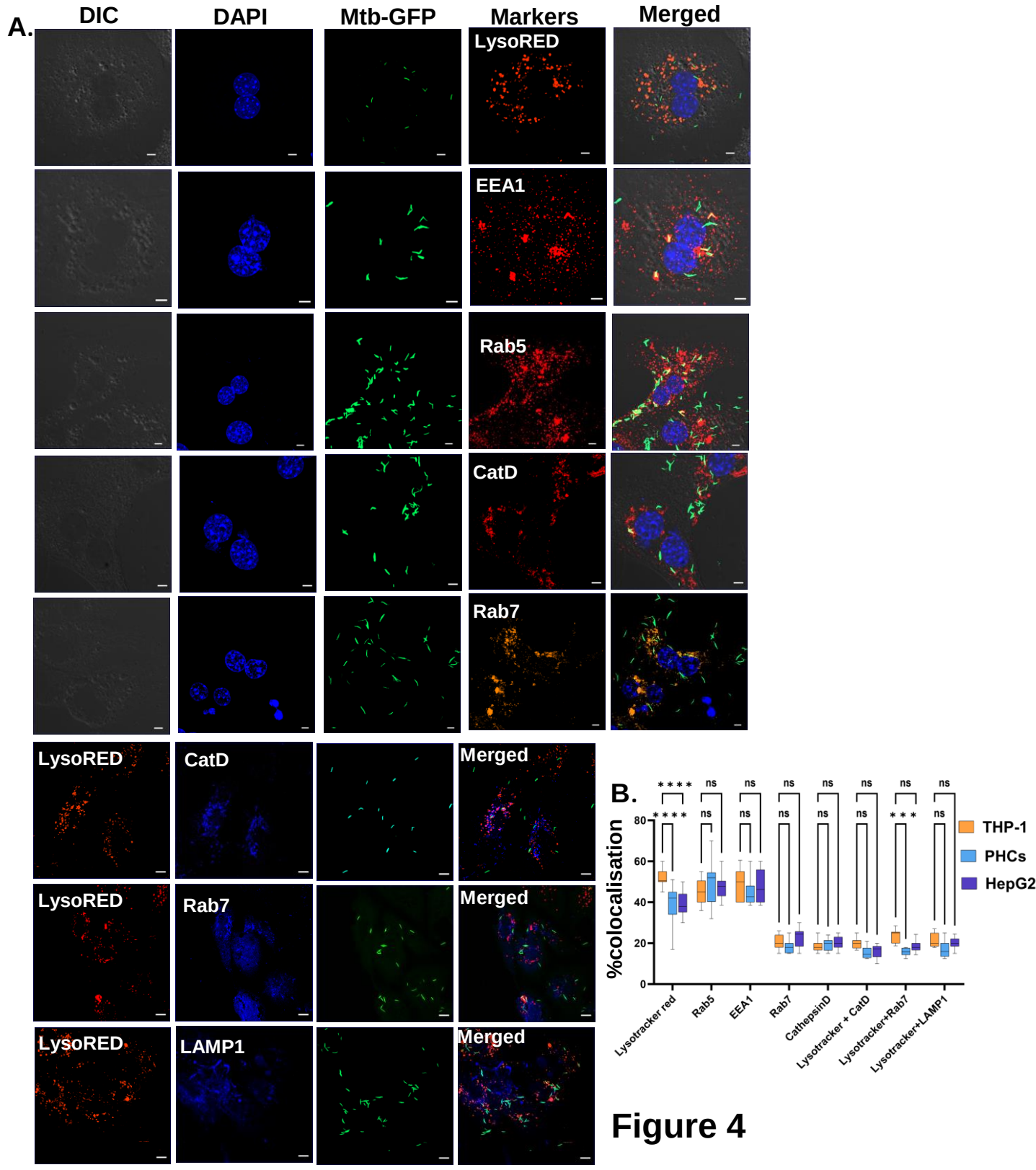
A.
DIC
DAPI
Mtb-GFP
Markers
Merged
LysoRED
EEA1
Rab5
CatD
Rab7
LysoRED
CatD
Merged
LysoRED
Rab7
Merged
LysoRED
LAMP1
Merged
B.
%colocalisation
80
60
40
20
0
* * * *
ns
* * *
THP-1
PHCs
HepG2
Lysotracker red
Rab5
EEA1
Rab7
CathepsinD
Lysotracker + CatD
Lysotracker+Rab7
Lysotracker+LAMP1

Figure 4

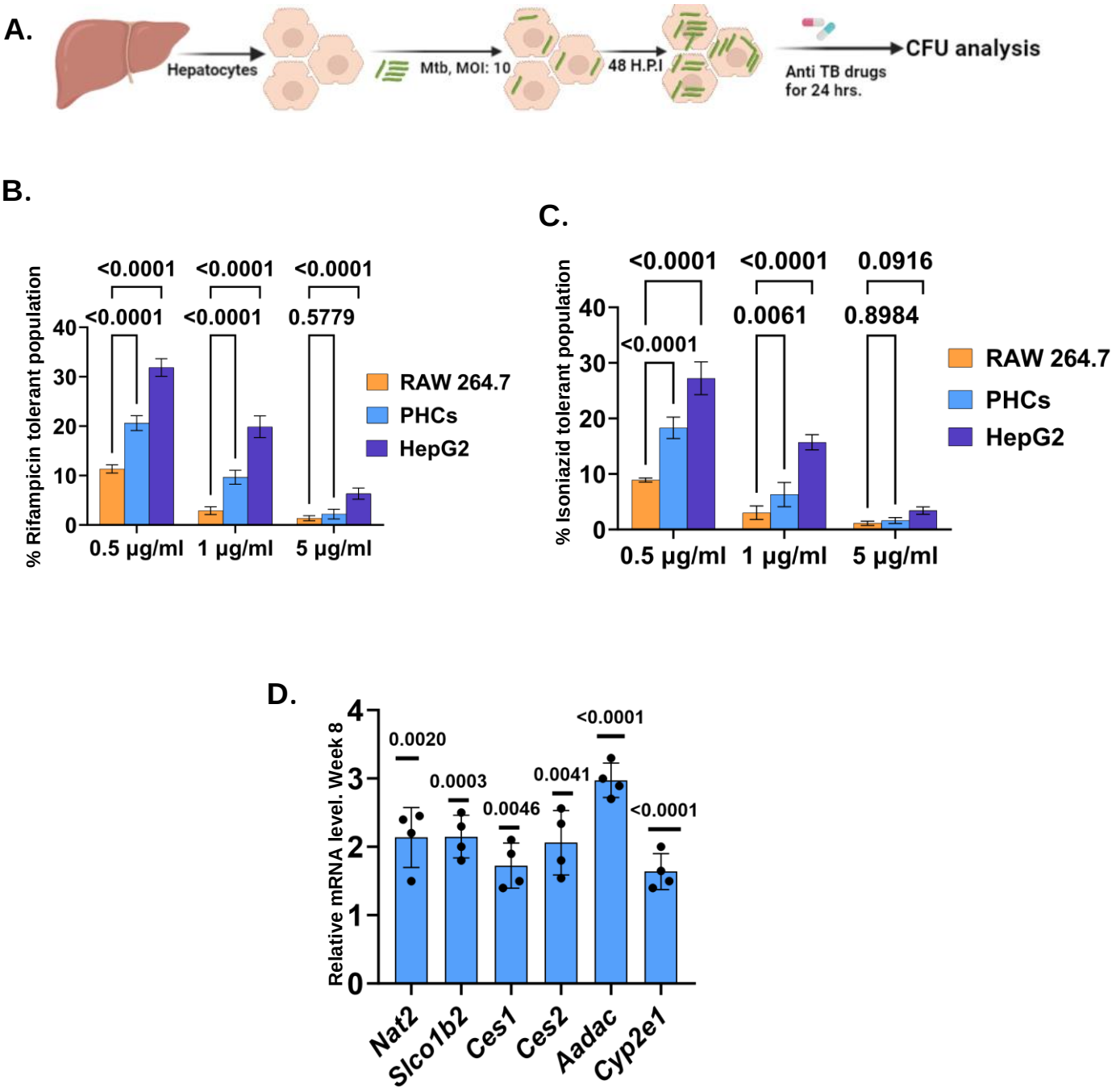
A.
Hepatocytes
Mtb, MOI: 10
48 H.P.I
Anti TB drugs
for 24 hrs.
CFU analysis
B.
% Rifampicin tolerant population
<0.0001
<0.0001
<0.0001
<0.0001
<0.0001
0.5779
0.5 µg/ml
1 µg/ml
5 µg/ml
RAW 264.7
PHCs
HepG2
C.
% Isoniazid tolerant population
<0.0001
<0.0001
0.0916
<0.0001
0.0061
0.8984
0.5 µg/ml
1 µg/ml
5 µg/ml
RAW 264.7
PHCs
HepG2
D.
Relative mRNA level. Week 8
0.0020
0.0003
0.0046
0.0041
<0.0001
<0.0001
Nat2
Slco1b2
Ces1
Ces2
Aadac
Cyp2e1

**Figure 5**

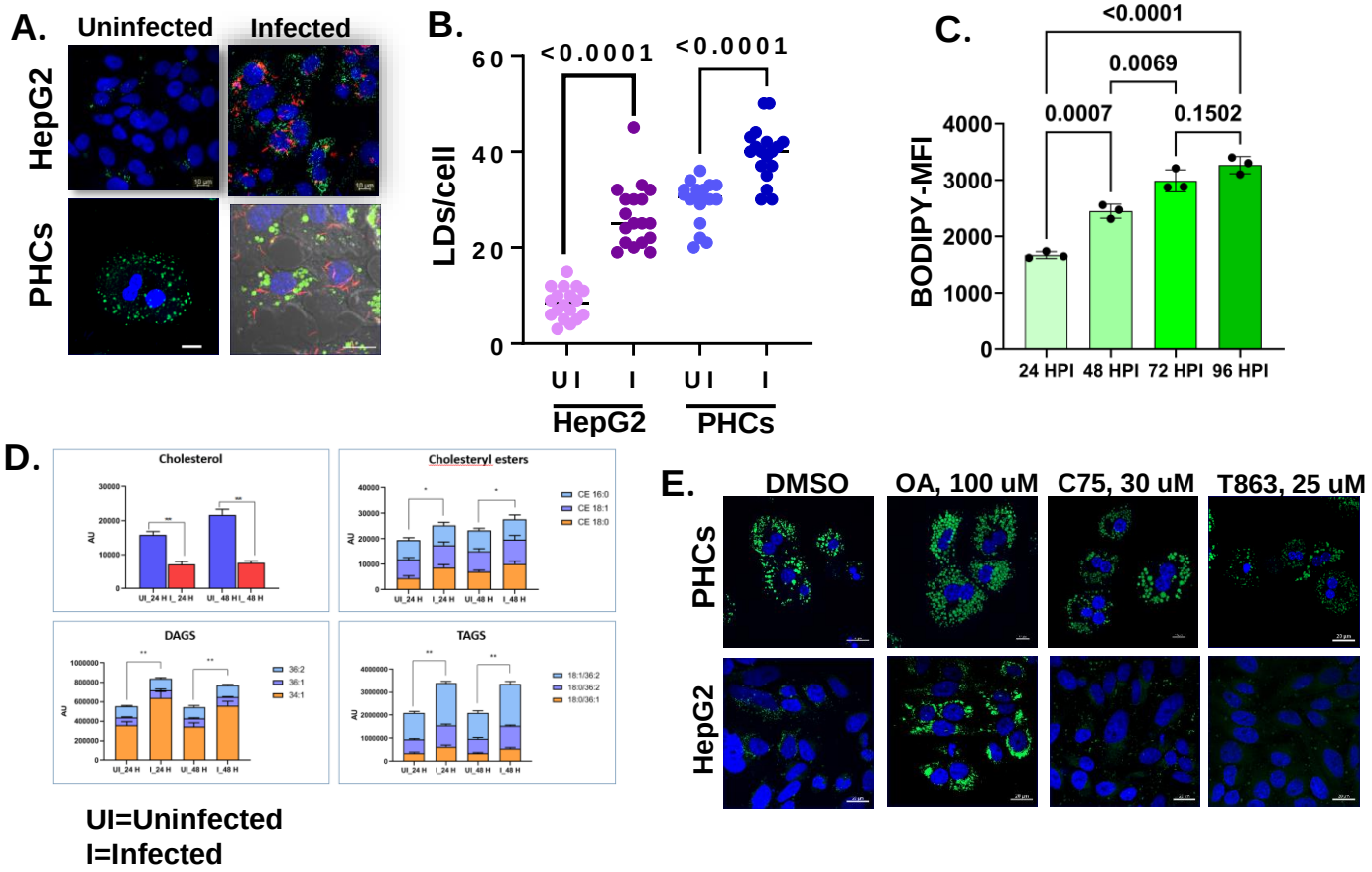
A.
Uninfected
Infected
HepG2
PHCs
B.
<0.0001
<0.0001
LDs/cell
60
40
20
0
UI
I
UI
I
HepG2
PHCs
C.
<0.0001
0.0069
0.0007
0.1502
BODIPY-MFI
4000
3000
2000
1000
0
24 HPI
48 HPI
72 HPI
96 HPI
D.
Cholesterol
Cholesteryl esters
DAGS
TAGS
UI=Uninfected
I=Infected
E.
DMSO
OA, 100 uM
C75, 30 uM
T863, 25 uM
PHCs
HepG2

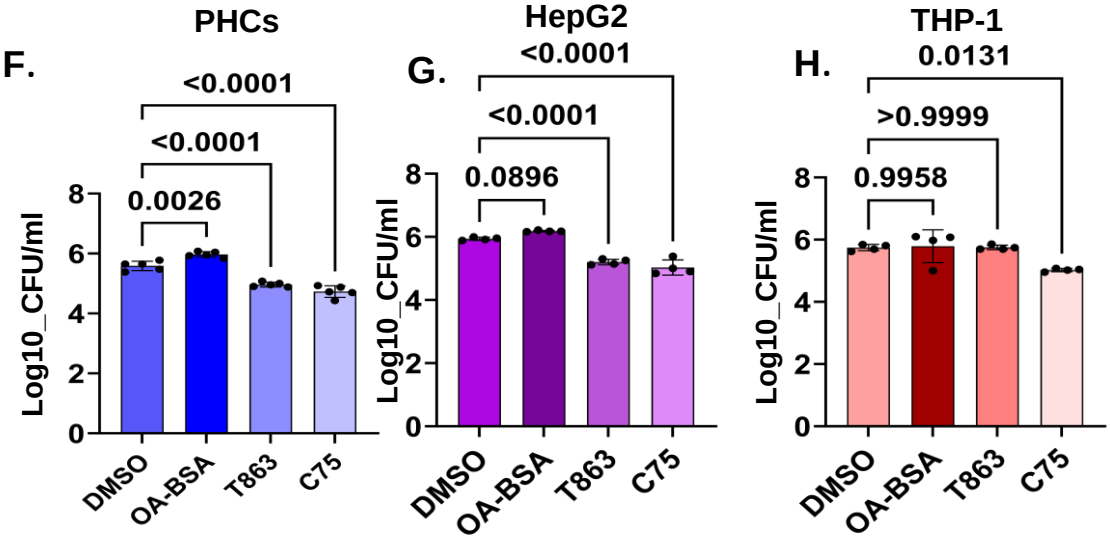
PHCs
F.
<0.0001
<0.0001
0.0026
Log10_CFU/ml
8
6
4
2
0
DMSO
OA-BSA
T863
C75
HepG2
G.
<0.0001
<0.0001
0.0896
Log10_CFU/ml
DMSO
OA-BSA
T863
C75
THP-1
H.
0.0131
>0.9999
0.9958
Log10_CFU/ml
DMSO
OA-BSA
T863
C75

**Figure 6**

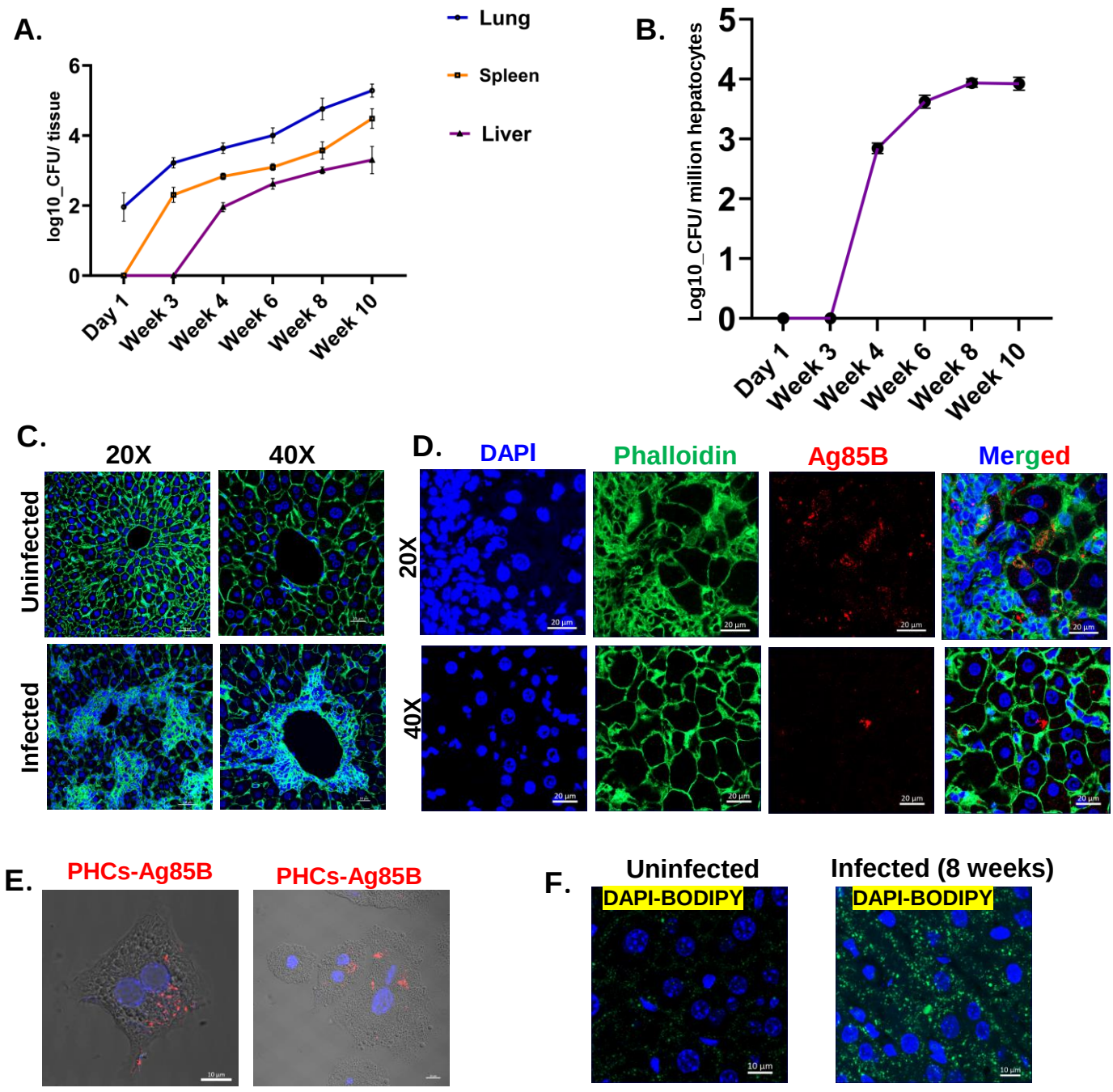
A.
Lung
Spleen
Liver
log10_CFU/ tissue
0
2
4
6
Day 1
Week 3
Week 4
Week 6
Week 8
Week 10
B.
Log10_CFU/ million hepatocytes
0
1
2
3
4
5
Day 1
Week 3
Week 4
Week 6
Week 8
Week 10
C.
20X
40X
Uninfected
Infected
D.
DAPI
Phalloidin
Ag85B
Merged
20X
40X
20 µm
E.
PHCs-Ag85B
PHCs-Ag85B
10 µm
F.
Uninfected
Infected (8 weeks)
DAPI-BODIPY
DAPI-BODIPY
10 µm

Figure 7

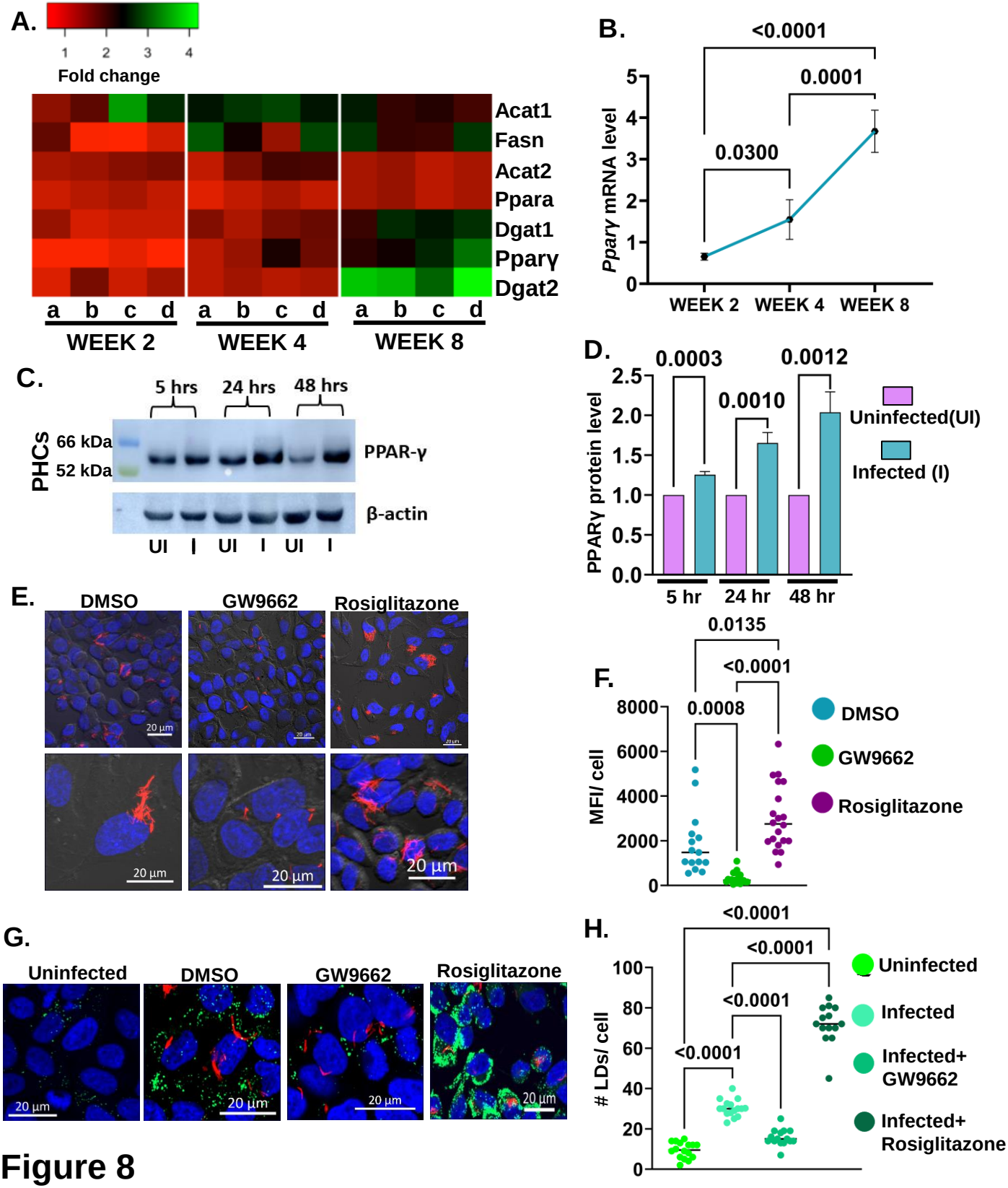
A.
1
2
3
4
Fold change
Acat1
Fasn
Acat2
Ppara
Dgat1
Pparγ
Dgat2
a b c d
a b c d
a b c d
WEEK 2
WEEK 4
WEEK 8
B.
<0.0001
0.0001
0.0300
Ppary mRNA level
0
1
2
3
4
5
WEEK 2
WEEK 4
WEEK 8
C.
5 hrs
24 hrs
48 hrs
PHCs
66 kDa
52 kDa
PPAR-γ
β-actin
UI I UI I UI I
D.
0.0003
0.0012
0.0010
PPARγ protein level
0.0
0.5
1.0
1.5
2.0
2.5
Uninfected(UI)
Infected (I)
5 hr
24 hr
48 hr
E.
DMSO
GW9662
Rosiglitazone
20 µm
F.
0.0135
<0.0001
0.0008
MFI/ cell
0
2000
4000
6000
8000
DMSO
GW9662
Rosiglitazone
G.
Uninfected
DMSO
GW9662
Rosiglitazone
20 µm
H.
<0.0001
<0.0001
<0.0001
<0.0001
# LDs/ cell
0
20
40
60
80
100
Uninfected
Infected
Infected+ GW9662
Infected+ Rosiglitazone

Figure 8